Role of muons in binary neutron star mergers: First simulations

Henrique Gieg,[1,*] Federico Schianchi,[1] Maximiliano Ujevic,[2] and Tim Dietrich[1,3]
[1]*Institut für Physik und Astronomie, Universität Potsdam, Haus 28, Karl-Liebknecht-Straße 24/25, 14476, Potsdam, Germany*
[2]*Centro de Ciências Naturais e Humanas, Universidade Federal do ABC, 09210-170, Santo André, São Paulo, Brazil*
[3]*Max Planck Institute for Gravitational Physics (Albert Einstein Institute), Am Mühlenberg 1, Potsdam 14476, Germany*

(Received 18 September 2024; revised 23 June 2025; accepted 1 July 2025; published 23 July 2025)

In this work, we present a set of binary neutron star (BNS) merger simulations including the net muon fraction as an additional degree of freedom in the equation of state (EOS) and hydrodynamics evolution using the numerical-relativity code BAM. Neutrino cooling is modeled via a neutrinos leakage scheme, including in-medium corrections to the opacities and emission rates of semileptonic charged-current reactions, although within the elastic approximation. We show that, for our particular choice of baseline baryonic EOS, the presence of muons delays the gravitational collapse of the remnant compared to the case where muons are neglected. Furthermore, when muons and muonic weak reactions are considered, no gravitational collapse occurs within our simulation time and muons are confined in the densest portions of the remnant, while the disk is effectively colder, less protonized and demuonized. Accordingly, ejecta properties are affected; e.g., ejecta masses are systematically smaller for the muonic setups and exhibit a larger fraction of neutron-rich, small velocity material. Overall, our results suggest that the inclusion of muons and muon-flavored neutrino reactions in the context of BNS merger simulations should not be neglected, thus representing an important step toward more realistic modeling of such systems.

DOI: 10.1103/52ph-53yw

I. INTRODUCTION

Merging binary neutron stars (BNS) are among the most prominent sources of multimessenger signals, which combine gravitational-wave (GW) measurements [1–3] with their associated electromagnetic (EM) counterparts, such as gamma-ray bursts [4–10] and kilonovae, e.g., AT2017gfo [11–16]. Such observations allow, for instance, one to constrain the uncertain equation of state (EOS) governing neutron-star matter at supranuclear densities [17–32], assess cosmological properties of the Universe [28,33–38], and study the formation of heavy elements [39–41].

The interpretation of multimessenger signatures produced during and after a BNS merger requires one to correlate theoretical predictions with the observed signatures. Due to the inherently nonlinear dynamics of such compact systems, numerical-relativity (NR) simulations are required to compute the emitted GWs and predict thermodynamical properties of matter along the postmerger. In binary neutron star (BNS) merger simulations, the state of the art involves efforts to realistically model the wide range of physical phenomena expected to occur under the extreme conditions present during the inspiral, merger, and postmerger phases. Some examples include accurate modeling of the matter and hydrodynamics [42–52], the role of magnetic fields [53–59], and the inclusion of neutrino transport [60–73].

One key assumption regarding the modeling of matter is that the EOS contains only electrons e^- and positrons e^+ as representative leptonic species. Hence, matter properties are described by EOSs that are represented as three-dimensional functions of the baryon rest-mass density ρ, temperature T, and net electron fraction Y_e. However, core-collapse supernovae simulations [74–76] show that muons μ^- and antimuons μ^+ are produced in non-negligible amounts via weak reactions during the formation of a neutron star (NS). Over larger timescales, when the matter cools and reaches the neutrinoless β equilibrium, muons are expected to be present wherever the electron chemical potential μ_e exceeds the muon rest mass m_μ, i.e., $\mu_e \geq m_\mu c^2 \approx 106$ MeV [77–80]. Hence, the description of matter encompassed by the EOS should include an additional degree of freedom, accounting for the net muon fraction Y_μ.

*Contact author: henrique.gieg@uni-potsdam.de

Published by the American Physical Society under the terms of the Creative Commons Attribution 4.0 International license. Further distribution of this work must maintain attribution to the author(s) and the published article's title, journal citation, and DOI.

Besides, it has been shown that the presence of muons in the interior of neutron stars leads to important microphysical consequences, e.g., the arise of bulk viscosity due to leptonic reactions [81–83], the modification of the direct Urca threshold [84], the occurrence of muon-flavored weak reactions, and an overall increased proton fraction in locally neutral, β-stable matter when compared to EOSs that include only e^- and e^+.

Interestingly, up to our knowledge, there are only two studies that address the possible impacts of considering muons in BNS systems. The first one is Ref. [85], which employs postprocessing of data from BNS merger simulations that were produced neglecting the presence of muons. Such a procedure provided important insights about the role of muons during the postmerger stage with respect to the hydrodynamics of matter and the behavior of neutrinos in the trapped regime. However, the method is not able to capture in details the complete dynamics and postmerger evolution of a BNS that is simulated *ab initio* including muons and treating the neutrinos-driven interactions on the fly. More recently, Ref. [86] performed BNS merger simulations without neutrinos transport, but including pions, muons, and trapped neutrinos in the EOS under the assumptions of (i) strong interaction equilibrium among negatively charged pions, neutrons, and protons, (ii) weak interaction equilibrium among neutrinos, leptons, and nucleons and (iii) a prescription for the muon-flavored number fraction as a function of the rest-mass density. Hence, their modified EOS is three-dimensional and does not account for the advection of muons. Nevertheless, important dynamical effects are noted, e.g., changes in the thermal and compositional profile of the remnant, in the ejecta properties, and in the postmerger GW frequencies.

In this work, we intend to surpass the shortcomings of previous investigations and present NR simulations of BNS mergers carried out with the inclusion of muons in the EOS and hydrodynamics and the use of a Neutrinos Leakage Scheme (NLS) to model the cooling of matter in response to the production of neutrinos, in particular, accounting for muon-flavored neutrinos. The structure of this paper is as follows: In Sec. II, we describe our procedures for the construction of EOSs including muons and the modifications of the general-relativistic hydrodynamics (GRHD) equations. In Sec. III, we present details about the NLS implementation and the computation of emissivities and opacities for set of weak reactions. In Sec. IV, we state our methods and BNS setups considered in this worked, which were evolved with the BAM code [47,49,59,72,87–89]. In Sec. V, we present a qualitative discussion about the merger and postmerger dynamics. In Sec. VI, we make an analysis of the ejecta properties. Finally, in Sec. VII, we state our concluding remarks. Throughout this work, we adopt units in which the gravitational constant G, the speed of light in vacuum c, the solar mass $M_\odot$, and the Boltzmann constant k_B are equal to one. Greek letters represent spacetime indices ranging from 0 to 3, while Latin letters are used for spacelike tensor and range from 1 to 3. The spacetime metric $g_{\mu\nu}$ has signature $(-,+,+,+)$.

II. EQUATION OF STATE AND HYDRODYNAMICS

Generally, a muonic EOS may be constructed by "dressing" a baseline baryonic EOS,[1] parametrized by the baryon number density n_b, temperature T, and charge fraction of strongly interacting particles Y_q with a leptonic EOS. In the following, we consider the leptons and the antileptons $l = \{e^-, \mu^-, e^+, \mu^+\}$ as relativistic ideal Fermi gases. Hence, the lepton number density $n_{l^\mp}$, energy density $\varepsilon_{l^\mp}$, and pressure $p_{l^\mp}$ read [90,91]

$$n_{l^\mp} = K_l \beta_l^{3/2} [F_{1/2}(\eta^0_{l^\mp}, \beta_l) + \beta_l F_{3/2}(\eta^0_{l^\mp}, \beta_l)], \quad (1)$$

$$\varepsilon_{l^\mp} = K_l m_l c^2 \beta_l^{5/2} [F_{3/2}(\eta^0_{l^\mp}, \beta_l) + \beta_l F_{5/2}(\eta^0_{l^\mp}, \beta_l)] + m_l c^2 n_{l^\mp}, \quad (2)$$

$$p_{l^\mp} = \frac{K_l m_l c^2}{3} \beta_l^{5/2} [2F_{3/2}(\eta^0_{l^\mp}, \beta_l) + \beta_l F_{5/2}(\eta^0_{l^\mp}, \beta_l)], \quad (3)$$

where m_l is the lepton rest mass, $\beta_l = T/m_l c^2$ is the relativity parameter, K_l is a constant

$$K_l = 8\pi\sqrt{2}(m_l c^2/hc)^3, \quad (4)$$

$\eta^0_{l^\mp}$ are the nonrelativistic degeneracy parameters

$$\eta^0_{l^-} = \frac{\mu_{l^-} - m_l c^2}{T}, \quad (5)$$

$$\eta^0_{l^+} = -\left(\eta^0_{l^-} + \frac{2}{\beta_l}\right), \quad (6)$$

and μ_{l^-} is the relativistic lepton chemical potential (including rest mass). Note that Eq. (5) is a definition, while Eq. (6) arises from the equilibrium between particles, antiparticles, and photons (with zero chemical potential). Finally, $F_k(\eta^0_{l^\mp}, \beta_l)$ is the generalized Fermi integral of order k, whose evaluation is performed numerically following [92].

The procedure to construct our complete EOS is presented in the following. The first step of our method consists in considering a baseline baryonic EOS parametrized by (n_b, T, Y_q), which is also taken as the baseline three-dimensional space for the addition of the leptonic sectors of the EOS. It is important to mention that in this work, we consider baseline baryonic models containing

[1]Such as those found, for example, in the CompOSE database https://compose.obspm.fr/.

only protons, neutrons, and nuclei. In this case, $Y_q = Y_p$, and we remark that, throughout this manuscript, Y_p stands for the free EOS parameter. Next, from Eqs. (1), (5), and (6), we define the net lepton fraction Y_l as

$$Y_l(n_b, T, \eta^0_{l^-}) = [n_{l^-}(\eta^0_{l^-}, T) - n_{l^+}(\eta^0_{l^+}, T)]/n_b, \quad (7)$$

which depends on (n_b, T) and on the nonrelativistic lepton degeneracy parameter $\eta^0_{l^\mp}$.

Hence, for each pair (n_b, T), Y_l is a function of $\eta^0_{l^-}$ alone. By choosing values of Y_l for a pair (n_b, T), which corresponds to fixing the triple (n_b, T, Y_l), $\eta^0_{l^-}$ may be recovered by numerically inverting Eq. (7), giving $\eta^0_{l^-} = \eta^0_{l^-}(n_b, T, Y_l)$. Consequently, the thermodynamical properties ξ_l associated to the lepton/antilepton gas, such as pressure, energy density, and entropy, also become functions of (n_b, T, Y_l), as

$$\begin{aligned}\xi_l &= \xi_{l^-}(T, \eta^0_{l^-}(n_b, T, Y_l)) + \xi_{l^+}(T, \eta^0_{l^+}(n_b, T, Y_l)) \\ &= \xi_{l^-}(n_b, T, Y_l) + \xi_{l^+}(n_b, T, Y_l). \end{aligned} \quad (8)$$

Then, for a chosen set of Y_l, a tabulated EOS may be produced in the parameter space (n_b, T, Y_l), representing a lepton/antilepton species.

More concretely, what we do is to choose a range of muon fractions $Y_\mu = [1 \times 10^{-4}, 1 \times 10^{-1}]$, logarithmically spaced with 20 points per decade, plus a $Y_\mu = 0$ slice, for a total of $N_{Y_\mu} = 62$ points. Then we tabulate an EOS for (anti)muons $\xi_\mu(n_b, T, Y_\mu)$ in the same parameter subspace (n_b, T) of the baseline baryonic EOS. Note that the (anti) muon EOS is completely independent of the baryonic sector. Still, it is possible to combine both sectors into one EOS by simply appending one dimension to any of the EOSs parameter spaces. Our choice is to add the Y_μ degree of freedom to the baseline baryonic EOS parameter space such that to each point (n_b, T, Y_p) corresponds N_{Y_μ} entries, promoting a three-dimensional EOS to the four dimensions (n_b, T, Y_p, Y_μ).

The next step is to produce a tabulated EOS for the electron/positron gas. Again, following the procedure previously outlined, one could freely choose a range of electron fractions Y_e consistent with (n_b, T) and produce an EOS for electrons/positrons, in principle, completely independent of the baryonic and muonic sectors. However, here we choose the Y_e values of our tabulation, enforcing charge neutrality at each point of the four-dimensional EOS parameter space; i.e., for each point (n_b, T, Y_p, Y_μ), we make

$$Y_e = Y_p - Y_\mu. \quad (9)$$

Then we solve Eq. (7) to obtain $\eta^0_{e^-} = \eta^0_{e^-}(n_b, T, Y_p, Y_\mu)$, which then sets the thermodynamical properties of the resulting electron/positron gas $\xi_e(T, \eta^0_{e^-}) = \xi_e(n_b, T, Y_e = Y_p - Y_\mu)$. Finally, we compute the pressure p and energy density ε of a fluid element by adding all species contributions (as well as contributions from photons γ), giving

$$\begin{aligned} p = {} & p_b(n_b, T, Y_p) + p_\mu(n_b, T, Y_\mu) \\ & + p_e(n_b, T, Y_e) + p_\gamma(T), \end{aligned} \quad (10)$$

$$\begin{aligned} \varepsilon = {} & \varepsilon_b(n_b, T, Y_p) + \varepsilon_\mu(n_b, T, Y_\mu) \\ & + \varepsilon_e(n_b, T, Y_e) + \varepsilon_\gamma(T), \end{aligned} \quad (11)$$

where

$$\varepsilon_\gamma = \frac{8\pi^5}{15}\frac{T^4}{(hc)^3}, \qquad p_\gamma = \varepsilon_\gamma/3 \quad (12)$$

correspond to the EOS of photons at zero chemical potential and in thermal equilibrium with the matter. Note that we neglect the pressure exerted by trapped neutrinos and their contribution to the matter energy density. See, e.g., [85,86,93] for investigations concerning the role of trapped neutrinos.

For the purposes of this work, there are two special cases of interest for the muonic EOS: The first one is when $Y_\mu = 0$, which trivially sets $\eta^0_{\mu^-} = \eta^0_{\mu^+} = -1/\beta_\mu$. The second one, relevant for the construction of initial data, comes by imposing the neutrinoless β-equilibrium condition for the reactions

$$n + \nu_l \leftrightarrow l^- + p. \quad (13)$$

In this case, the neutrino chemical potential vanishes, and the lepton chemical potentials are given by

$$\begin{aligned} \mu_e(n_b, T, Y_p) &= \mu_\mu(n_b, T, Y_p) \\ &= \mu_n(n_b, T, Y_p) - \mu_p(n_b, T, Y_p). \end{aligned} \quad (14)$$

Setting a constant temperature $T = T_0$, e.g., the lowest tabulated temperature of the baryonic EOS, Eq. (9) is solved for each n_b along with Eq. (14) for Y_p. Then, adding the leptons and photons contributions according to Eqs. (2), (3), a one-dimensional cold, neutrinoless β-equilibrated EOS is produced. It is worth pointing out that this EOS is employed only for the construction of initial data, while the full three-dimensional or four-dimensional EOSs are employed during the dynamical evolution. Obviously, for simulations without muons, the one-dimensional, neutrinoless β-equilibrated EOS is obtained by fixing $T = T_0$ and solving

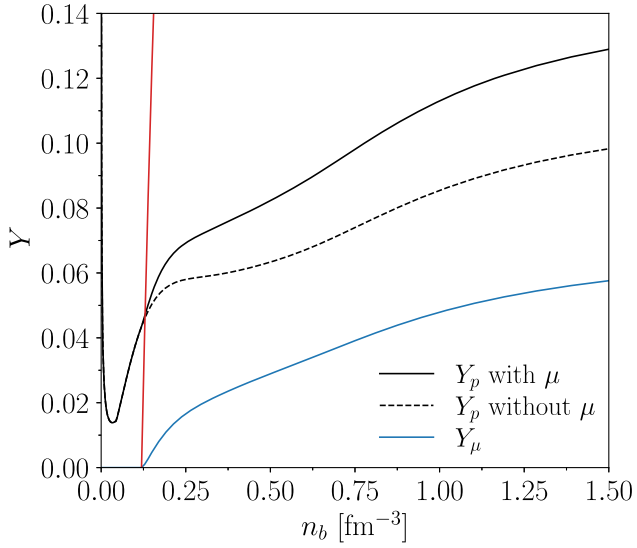


FIG. 1. Proton fraction for a cold, β-equilibrated slice of the SFHo EOS with muons (black thick line), its correspondent muon fraction (blue thick line), and the proton fraction without muons (black dashed line) as a function of the baryonic number density n_b. The red vertical line represents the fractional difference $(\mu_e - m_\mu c^2)/(m_\mu c^2)$. For $\mu_e \geq m_\mu c^2$, muons are present.

$$\mu_e(n_b, T_0, Y_p) = \mu_n(n_b, T_0, Y_p) - \mu_p(n_b, T_0, Y_p),$$
$$Y_e = Y_p.$$

To illustrate the changes introduced by the presence of muons in the composition of the matter, we depict in Fig. 1 the proton and muon fraction for a cold $T = 0.1$ MeV, β-equilibrated muonic EOS, adopting the SFHo baryonic EOS [94]. For small baryon densities $n_b \lesssim 0.125$ fm^{-3}, the muonic (thick black line) and electronic (dashed black line) EOSs have the same proton fraction. Once $\mu_e \geq m_\mu c^2$ (which is represented by the red line), muons are present within the matter ($Y_\mu > 0$), and, accordingly, due to the local charge neutrality condition, the proton fraction becomes larger for the muonic EOS by a factor of at most 31% at $n_b = 1.5$ fm^{-3}. It should be noted that this leads to a slight decrease of internal energy compared to when muons are absent because of (i) the conversion of electrons into muons and the subsequent loss of electron degeneracy energy by deoccupation of energy levels, which is consistent with the (small) reduction of the electron chemical potential when muons are present, and (ii) the larger proton fraction leads to a loss of the neutron energy contribution to the internal energy. However, since muons only appear at moderately high densities, where the baryonic pressure and energy density dominate over the leptonic contributions, the impact of muons in macroscopic properties of a cold NS (e.g., mass, radius, and tidal deformability) is negligible.

As for the initial data used in our BNS simulations, we present in Fig. 2 one-dimensional profiles along the x axis (in simulation coordinates, where here we adapt $x = 0$ to coincide with the center of the NS) of the pressure and particle fractions for the initial data employed in our simulations. As anticipated, for cold, catalyzed matter, the pressure (upper panel) is slightly larger around the center of the NS when muons are absent (dashed lines) due to the increased neutron degeneracy pressure in a more neutron-rich medium, indicated by the overall smaller proton fraction in the NS interior (dashed black line in the lower panel). Furthermore, Y_p decreases outward until the interface with the artificial atmosphere adopted in our simulations is reached, which is marked by an increase in Y_p to $\sim$0.46 (set by the β-equilibrium condition at the minimum tabulated temperature and density). Finally, for the EOS containing muons, the muon fraction (thick blue

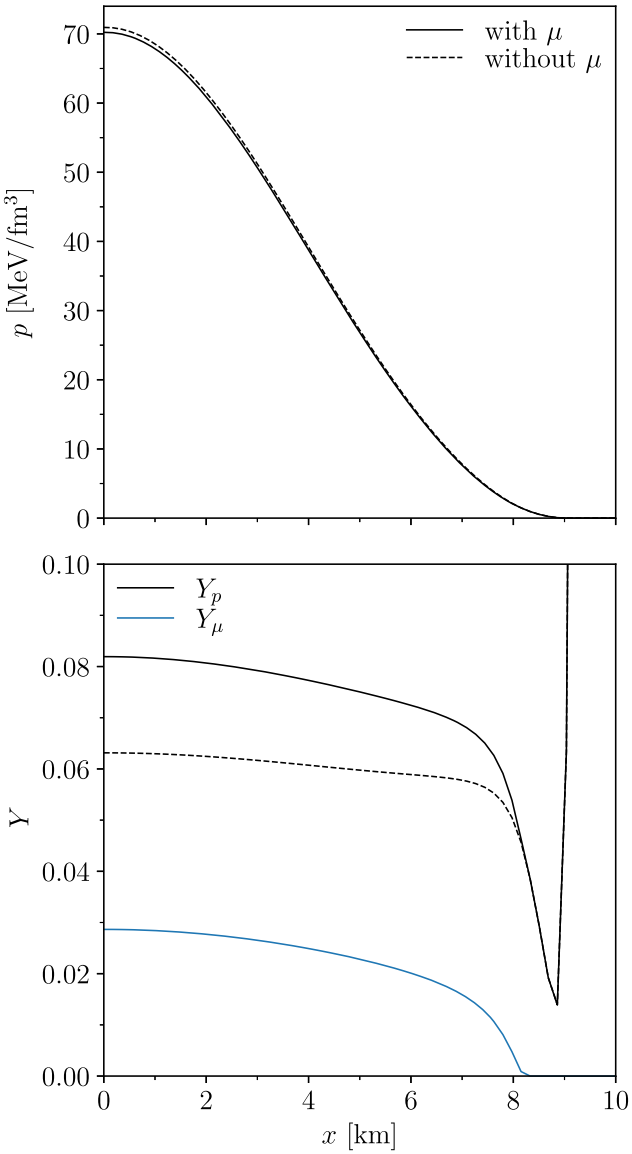


FIG. 2. Pressure (upper panel) and particle fractions (lower panel) observed in the initial data with (thick lines) and without (dashed lines) muons.

line in the lower panel) decreases smoothly toward the edge of the NS, leaving a muonless layer of ∼1 km.

In the following, we summarize relevant information regarding the EOS used in this work. For comparison purposes with results from the literature, we adopt the SFHo baseline EOSs. The baryon mass constant is chosen as $m_b = 1.659 \times 10^{-24}$ g, and the rest-mass density is given by $\rho = m_b n_b$. The range of validity for the EOS parameters are $\rho = [1.695 \times 10^3, 2.489 \times 10^{15}]$ g/cm^3, equispaced in log scale with 30 points per decade, $T = [0.1, 120]$ MeV, equispaced in log scale with 30 points per decade, $Y_p = [0.01, 0.60]$ equispaced in linear scale with stride 0.01 and $Y_\mu = [1 \times 10^{-4}, 1 \times 10^{-1}]$, equispaced in log scale with 20 points per decade plus $Y_\mu = 0$, for a total of 62 points in the Y_μ dimension. All necessary thermodynamical information is obtained by means of a quadrilinear interpolation over the aforementioned EOS validity region. For such a parametrization choice, the 3 + 1 form of the GRHD equations of [95] are the same as in [96] for the conserved rest-mass density D, internal energy density τ, and momentum density S_i, but here, we evolve Y_p and Y_μ according to

$$\partial_0(\sqrt{\gamma}DY_p) + \partial_i[\sqrt{\gamma}DY_p(\alpha v^i - \beta^i)] = \alpha\sqrt{\gamma}S_{Y_p}, \quad (15)$$

$$\partial_0(\sqrt{\gamma}DY_\mu) + \partial_i[\sqrt{\gamma}DY_\mu(\alpha v^i - \beta^i)] = \alpha\sqrt{\gamma}S_{Y_\mu}, \quad (16)$$

where γ is the determinant of the spatial metric, α is the lapse function, β^i is the shift vector, v^i is the three-velocity measured in the Eulerian frame, and S_{Y_p} and S_{Y_μ} are source terms that we introduce in the next section. The extension of our previous high-resolution shock-capturing (HRSC) scheme [89] to the present case is straightforward.

III. NEUTRINOS LEAKAGE SCHEME

A. A brief overview

The NLS [60–62,69,96–106] is a simplified method to account for cooling produced by neutrino irradiation, devised to obtain order-of-magnitude estimates of the role of neutrinos in astrophysical scenarios without resorting to approximate solutions of the Boltzmann equation, such as moments-based schemes [63,67,68,71,107,108], Monte-Carlo schemes [109–111], and lattice-Boltzmann transport schemes [112]. Differently than in previous BNS merger studies, instead of three neutrino species $\{\nu_e, \bar{\nu}_e, \nu_x\}$, we also consider five neutrino species $\{\nu_e, \bar{\nu}_e, \nu_\mu, \bar{\nu}_\mu, \nu_x\}$, where the heavy lepton neutrinos $\nu_x = \{\nu_\tau, \bar{\nu}_\tau\}$ are grouped as a single species with statistical weight 2. In the following, neutrinos are assumed to be governed by the ultrarelativistic Fermi-Dirac distribution in local thermal and β equilibrium with the matter [61]; i.e., the degeneracy parameters read

$$\eta_{\nu_e} = (\mu_p + \mu_e - \mu_n)/T, \qquad \eta_{\bar{\nu}_e} = -\eta_{\nu_e}, \quad (17)$$

$$\eta_{\nu_\mu} = (\mu_p + \mu_\mu - \mu_n)/T, \qquad \eta_{\bar{\nu}_\mu} = -\eta_{\nu_\mu}, \quad (18)$$

$$\eta_{\nu_x} = 0, \quad (19)$$

where the above chemical potentials include rest mass.

The NLS prescription adopted in this work assumes that the energy-momentum conservation applied to a matter element is modified according to

$$\nabla_\nu T^{\mu\nu}_{\text{matter}} = -\mathcal{Q}u^\mu, \quad (20)$$

where ∇_ν is the covariant derivative compatible with the spacetime metric $g_{\mu\nu}$, $T^{\mu\nu}_{\text{matter}}$ is the stress-energy tensor of matter, considered here as an ideal fluid, u^μ is the four-velocity of the matter element, and $\mathcal{Q}$ is the total effective energy production rate, given by the sum of effective energy production rates from each neutrino species $Q^{\text{eff}}_I, I = \{\nu_e, \bar{\nu}_e, \nu_\mu, \bar{\nu}_\mu, \nu_x\}$

$$\mathcal{Q} = \sum_I Q^{\text{eff}}_I. \quad (21)$$

As stated, the standard NLS only accounts for the cooling of the matter by emission of neutrinos, while absorption and advection of neutrinos are not considered. On the other hand, since neutrinos are leptons, the set of considered neutrinos-driven reactions consistently modify the lepton family number conservation laws as

$$\nabla_\nu(\rho Y_e u^\nu) = S_{Y_e}, \quad (22)$$

$$\nabla_\nu(\rho Y_\mu u^\nu) = S_{Y_\mu}, \quad (23)$$

while the baryon number conservation law reads

$$\nabla_\nu(\rho u^\nu) = 0. \quad (24)$$

In face of the above equation, Eqs. (22), (23) become, respectively,

$$S_{Y_e} = \rho u^\nu \nabla_\nu(Y_e) = \rho \frac{dY_e}{d\tau} \equiv m_b(R^{\text{eff}}_{\bar{\nu}_e} - R^{\text{eff}}_{\nu_e}), \quad (25)$$

$$S_{Y_\mu} = \rho u^\nu \nabla_\nu(Y_\mu) = \rho \frac{dY_\mu}{d\tau} \equiv m_b(R^{\text{eff}}_{\bar{\nu}_\mu} - R^{\text{eff}}_{\nu_\mu}), \quad (26)$$

where $d/d\tau$ is the derivative with respect to the proper time of a fluid element. Hence, R^{eff}_I is interpreted as the effective particle production rate of I in the fluid rest frame. Finally, applying the local charge neutrality condition Eq. (9), the source term for Y_p in Eq. (15) reads

$$S_{Y_p} = S_{Y_e} + S_{Y_\mu} = m_b(R^{\rm eff}_{\bar\nu_e} - R^{\rm eff}_{\nu_e} + R^{\rm eff}_{\bar\nu_\mu} - R^{\rm eff}_{\nu_\mu}). \quad (27)$$

Note that in our scheme, Y_p is evolved instead of Y_e via Eq. (15) with source term Eq. (27).

Following [60,70,104,106], the effective energy and particle production rates are computed, respectively, according to

$$Q^{\rm eff}_I = Q_I(1 + t^{\rm diff}_{I,1}/t^{\rm prod}_{I,1})^{-1}, \quad (28)$$

$$R^{\rm eff}_I = R_I(1 + t^{\rm diff}_{I,0}/t^{\rm prod}_{I,0})^{-1}, \quad (29)$$

where Q_I, R_I are the free energy and particle production rates, the production timescales are

$$t^{\rm prod}_{I,1} = B_{I,1}/Q_I, \qquad t^{\rm prod}_{I,0} = B_{I,0}/R_I, \quad (30)$$

with the neutrino energy density $B_{I,1}$

$$B_{I,1} = g_I \frac{4\pi}{(hc)^3} T^4 F_3(\eta_I), \quad (31)$$

the neutrino number density $B_{I,0}$

$$B_{I,0} = g_I \frac{4\pi}{(hc)^3} T^3 F_2(\eta_I), \quad (32)$$

$F_k(\eta_I)$ the ultrarelativistic Fermi integral of order k, and the degeneracy factors $g_{\nu_e} = g_{\bar\nu_e} = g_{\nu_\mu} = g_{\bar\nu_\mu} = 1$, $g_{\nu_x} = 2$ ($g_{\nu_x} = 4$) for five (three) neutrinos species. Note that given a set of reactions that produce neutrinos, all the aforementioned quantities may be estimated within our approach by direct interpolation from the EOS since thermal and chemical equilibrium is assumed.

However, the estimation of the diffusion timescale $t^{\rm diff}_{I,0}$ ($t^{\rm diff}_{I,1}$) is more involved since it depends on the local number-averaged opacitiy $\kappa_{I,0}$ (energy-averaged opacity $\kappa_{I,1}$), and on the nonlocal optical depth $\tau_{I,0}$ ($\tau_{I,1}$) according to

$$t^{\rm diff}_{I,j} = \frac{\mathcal{D}\tau^2_{I,j}}{c\kappa_{I,j}}, \qquad j = \{0,1\}, \quad (33)$$

with $\mathcal{D} = 6$ chosen following [97]. For future convenience, we define here the I neutrino sphere as the surface where $\tau_{I,j} = 1$, which represents the location outside of which neutrinos are effectively decoupled from matter [113].

The optical depths are estimated following the iterative procedure of Ref. [114]; i.e., during the initial time step, the optical depths are iterated until convergence for all grid points. During the evolution, optical depths are recomputed at each point once per time step by a single iteration using the optical depths from the previous time step. An alternative approach, based on the solution of the Eikonal equation for the optical depths, may be found in Ref. [115].

TABLE I. Weak reactions considered in this work. All the charged-current processes are computed within the elastic approximation. Note that for pair processes and elastic scatterings, neutrinos of all species may participate.

	References
Charged-current processes	
$\nu_e + n \leftrightarrow p + e^-$	[76,116]
$\bar\nu_e + p \leftrightarrow n + e^+$	[76,116]
$\nu_\mu + n \leftrightarrow p + \mu^-$	[76,116]
$\bar\nu_\mu + p \leftrightarrow n + \mu^+$	[76,116]
Pair processes	
$e^- + e^+ \to \nu + \bar\nu$	[60,117]
$\gamma \to \nu + \bar\nu$	[60,117]
Elastic scattering	
$\nu + p \to \nu + p$	[60,96]
$\nu + n \to \nu + n$	[60,96]
$\nu + A \to \nu + A$	[105]

In the following, we present in details the methods employed for the computation of opacities and emission rates for the processes considered in this work, which are summarized in Table I.

B. Opacities computation

A crucial part of modeling neutrino interactions consists of the evaluation of opacities associated with scattering and absorption reactions. As will become clear, a few differences are found between our opacities estimates and the widely adopted prescription for BNS studies, originally due to Ref. [60]. Instead, we closely follow Refs. [76,118].

We begin by considering that the charged-current (CC) absorption processes of Table I may be generically represented as

$$\nu + N_1 \to l + N_2, \quad (34)$$

which corresponds to the absorption of a neutrino ν by the nucleon N_1, yielding the lepton l and the nucleon N_2, where $N_1, N_2 = \{n, p\}$.

For simplicity, we restrict to modeling such reactions by means of the elastic approximation, i.e., neglecting the momentum transferred to nucleons by neutrinos. In this case, the absorption opacity is given by [76,116,118,119]

$$\kappa^{\rm abs}_I(\epsilon) = \frac{\sigma_0 V^2_{\rm ud}}{(m_e c^2)^2}\frac{(1+3g_A^2)}{4}(\epsilon+Q)^2\sqrt{1-\left(\frac{m_l c^2}{\epsilon+Q}\right)^2} \times [1 - f_l(\epsilon+Q)]\eta_{12}, \quad (35)$$

where $I = \{\nu_e, \bar\nu_e, \nu_\mu, \bar\nu_\mu, \nu_x\}$, $\kappa^{\rm abs}_{\nu_x}(\epsilon) = 0$, ϵ is the incoming neutrino energy, the reference cross-section

$$\sigma_0 = \frac{4G_F^2(m_e c^2)^2}{\pi(\hbar c)^4} \approx 1.761 \times 10^{-44}\ \mathrm{cm}^2, \tag{36}$$

$G_F = 1.1664 \times 10^{-5}\ \mathrm{GeV}^{-2}$ is the Fermi constant (in units of $\hbar = c = 1$), $V_{\mathrm{ud}} = 0.9742$ is the up-down entry of the Cabibbo-Kobayashi-Maskawa matrix [120], the axial coupling constant is $g_A \approx 1.27$, $E_l = \epsilon + Q$ is the energy of the lepton l, and the medium-modified Q value is

$$Q = m_1^* c^2 + U_1 - m_2^* c^2 - U_2,$$

where $m_{1/2}^*$ is the effective mass, and $U_{1/2}$ is the single-particle vector-interaction potential of $N_{1/2}$, generally provided by the EOS. Otherwise, estimates of U may be obtained following the procedure of [121]. The lepton distribution function f_l is the Fermi-Dirac function

$$f_l(\epsilon + Q) = \frac{1}{1 + \exp[(\epsilon + Q)/T - \eta_l]}, \tag{37}$$

and the nucleon phase-space blocking factor η_{12} is

$$\eta_{12} = \frac{n_2 - n_1}{\exp[(\mu_2 - \mu_1 + Q)/T] - 1}, \tag{38}$$

where $n_{1/2}$ is the number density of free nucleons, and $\mu_{1/2}$ is the nucleon chemical potential (including rest mass).

To avoid unphysical behavior of η_{12} in the nondegenerate regime, we follow the prescription found in [122] and set

$$\eta_{np} = n_n, \tag{39}$$

$$\eta_{pn} = n_p, \tag{40}$$

if $\mu_n - \mu_p - Q < 0.01$ MeV. Note that, although no other corrections are considered, we include in-medium effects in the limited kinematics of the absorption reaction Eq. (34) by means of the medium-modified Q factor.

The next step, common to all energy-independent schemes, is to consider the spectral average of the absorption opacity Eq. (35). To do so, the usual procedure consists is dropping the square root term in Eq. (35), which is equivalent to state that the energy of the outcoming lepton $E_l \gg m_l c^2$, i.e., that the produced leptons are ultrarelativistic. This is reasonable for electrons, since in general $Q > m_e c^2$, but for the case of muons, due to their substantially larger rest mass, such an approximation is not adequate.

Instead, we keep the square-root term but follow [60,105] and approximate the lepton phase-space blocking through averaging the energy $\bar{E}_l$ of the produced lepton via reaction Eq. (34)

$$[1 - f_l(\epsilon + Q)] \approx \langle 1 - f_l(\bar{E}_l)\rangle = \{1 + \exp[-(\bar{E}_l/T - \eta_l)]\}^{-1}. \tag{41}$$

Hence, the spectrally averaged absorption opacity reads

$$\kappa_{I,j}^{\mathrm{abs}} = \frac{1}{B_{I,j}} \langle 1 - f_l(\bar{E}_l)\rangle \frac{\sigma_0 V_{\mathrm{ud}}^2}{(m_e c^2)^2} \frac{(1 + 3g_A^2)}{4} \eta_{12} \mathcal{I}_{I,j}, \tag{42}$$

which is written in terms of the integral

$$\mathcal{I}_{I,j}(m_l, Q, T, \eta_I) = \frac{4\pi}{(hc)^3} T^{5+j} \int_{x_{\min}}^{\infty} (x + Q/T)^2 \sqrt{1 - \left(\frac{m_l c^2}{xT + Q}\right)^2}\, x^{2+j} f_I(x)\, dx. \tag{43}$$

In Eq. (43), the lower integration limit is $x_{\min} = \max[0, (m_l c^2 - Q)/T]$, which ensures that (i) the square-root term is real and (ii) that only neutrinos with energies larger than $m_l c^2 - Q > 0$ are absorbed. Naturally, $f_I(x)$ is the ultrarelativistic Fermi Dirac distribution function describing neutrinos, i.e.,

$$f_I(x) = \frac{1}{1 + \exp(x - \eta_I)}. \tag{44}$$

Before proceeding to the methods employed to perform the integral Eq. (43), we are in the position of defining the average energy of the produced lepton $\bar{E}_l$ by noting that the average energy of the absorbed neutrinos may be estimated as

$$\bar{E}_I = \kappa_{I,1}^{\mathrm{abs}} / \kappa_{I,0}^{\mathrm{abs}} = T(\mathcal{I}_{I,1}/\mathcal{I}_{I,0}). \tag{45}$$

Thus, energy conservation implies

$$\bar{E}_l = T \frac{\mathcal{I}_{I,1}}{\mathcal{I}_{I,0}} + Q. \tag{46}$$

We verified that such a prescription, along with the lower integration bound $x_{\min}$ defined later, ensures that $\bar{E}_l \geq m_l c^2$. It is straightforward to verify that when the square-root term of the integral Eq. (43) is neglected, one recovers Eq. (B13) of Ref. [105] from Eq. (42). Furthermore, neglecting Q, one recovers the widely adopted estimate of Ref. [60]

$$\bar{E}_l = T \frac{F_5(\eta_I)}{F_4(\eta_I)}.$$

So far, we have restated the problem of computing opacities as that of evaluating the integral Eq. (43). The current, widely adopted procedure of neglecting the square-root term and the Q factor have the clear advantage of

reducing the problem to the evaluation of the ultrarelativistic Fermi-Dirac integral, which is easily computed along a simulation given the pair (T, η_I) by means of, e.g., the sufficiently accurate formulas of Ref. [123]. However, as said, such an approach is not justified when applied to muonic weak reactions.

On the other hand, the numerical integration of Eq. (43) on the fly is computationally intensive since it may take up to hundreds of function evaluations per integral. Therefore, we resort to a precomputation of the integrals as to produce, from the EOS as input, a table of spectrally averaged opacities and emission rates parametrized by (ρ, T, Y_p, Y_μ), which are then used to compute opacities and emission rates along our simulations by means of quadrilinear interpolations.

Therefore, for each EOS point (ρ, T, Y_p, Y_μ), the integration of Eq. (43) is performed by adaptive quadratures up to desired accuracy with the double exponential method [124] as implemented in Refs. [125,126]. Naturally, modifications concerning the kernel of the integral and the lower integration boundary are in order since the original method is devised to integrate moments of the Fermi-Dirac distribution from $x_{\min} = 0$, which can be handled by simple variable transformations.

More specifically, we first distinguish two cases:

(i) If $m_l c^2 - Q \leq 0$, we integrate Eq. (43) with $x_{\min} = 0$ since neutrinos with all energies may participate in the reaction. The I degeneracy $\bar{\eta}_I = \eta_I$ and distribution function $\bar{f}_I(x) = f_I(x)$ remain unchanged.

(ii) If $m_l c^2 - Q > 0$, we make $\epsilon + Q = E + m_l c^2$ and $x = E/T$. The I degeneracy is thus rescaled by the transformation such that

$$\tilde{\eta}_I = \eta_I - \frac{(m_l c^2 - Q)}{T}, \tag{47}$$

$$\tilde{f}_I(x) = \frac{1}{1 + \exp(x - \tilde{\eta}_I)}, \tag{48}$$

and the integral Eq. (43) becomes

$$\tilde{\mathcal{I}}_{I,j} = \frac{4\pi}{(hc)^3} T^{5+j} \int_0^\infty (x + m_l c^2/T)^2 \sqrt{1 - \left(\frac{m_l c^2}{xT + m_l c^2}\right)^2} \times \left(x + \frac{m_l c^2 - Q}{T}\right)^{2+j} \tilde{f}_I(x) dx, \tag{49}$$

where we omitted the dependencies of $\tilde{\mathcal{I}}_{I,j}$ for a shorter notation.

One last limit has to be considered when computing Eq. (42): The black-body function $B_{I,j}$ may be evaluated to zero, which generally occurs for very negative neutrino degeneracies, although the ratio $\mathcal{I}_{I,j}/B_{I,j}$ is finite. Thus, in order to circumvent such a possible issue, we first compute the black-body functions $B_{I,0}, B_{I,1}$. If one of those functions evaluate to zero, we make

$$B_{I,j} = \frac{4\pi}{(hc)^3} T^{3+j} \exp(\eta_I)(2 + j)!, \tag{50}$$

which comes from expanding $f_I(x) \approx \exp(\eta_I)\exp(-x)$ for $\exp(\eta_I) \ll 1$.

On the other hand, when $\eta_I \leq -100$ (for $m_l c^2 - Q \leq 0$) or $\bar{\eta}_I \leq -100$ (for $m_l c^2 - Q > 0$), we proceed to similar expansions

$$f_I(x) \approx \exp(\eta_I)\exp(-x), \tag{51}$$

$$\bar{f}_I(x) \approx \exp(\bar{\eta}_I)\exp(-x), \tag{52}$$

and carry out the integrations Eqs. (43) or (49) with a 64-point Gauss-Laguerre quadrature. By doing so, we have explicitly factored out the $\exp(\eta_I)$ term that may drive $B_{I,j} \to 0$, thus allowing the computation of finite ratios $\mathcal{I}_{I,j}/B_{I,j}$.

Finally, for the elastic scattering of neutrinos ν in free nucleons N and heavy nuclei A

$$\nu + N \to \nu + N, \tag{53}$$

$$\nu + A \to \nu + A, \tag{54}$$

we compute the respective scattering opacities $\kappa^{\text{scatt}}_{I,j}(N)$ according to [96] and $\kappa^{\text{scatt}}_{I,j}(A)$ according to [105]. Hence, the opacities used in Eq. (33) and for the computation of optical depths is simply the sum of the opacities over all processes, i.e.,

$$\kappa_{I,j} = \kappa^{\text{abs}}_{I,j} + \kappa^{\text{scatt}}_{I,j}(n) + \kappa^{\text{scatt}}_{I,j}(p) + \kappa^{\text{scatt}}_{I,j}(A), \tag{55}$$

with $\kappa^{\text{abs}}_{\nu_x,j} = 0$.

C. Emission rates computation

For the emission via charged-current processes, we consider the inverse of the reaction presented in Eq. (34). Following [119], detailed balance sets the spectrally averaged emission rates as

$$Q^{\text{CC}}_{I,j} = \langle 1 - f_I(\bar{E}_I)\rangle \frac{\sigma_0 V^2_{\text{ud}} c}{(m_e c^2)^2} \frac{(1 + 3g_A^2)}{4} \eta_{21} \mathcal{I}^*_{I,j}, \tag{56}$$

where the integral $\mathcal{I}^*_{I,j}$ reads

$$\mathcal{I}^*_{I,j}(m_l, Q, T, \eta_l) = \frac{4\pi}{(hc)^3} T^{5+j} \int_{x_{\min}}^{\infty} (x + Q/T)^2 \times \sqrt{1 - \left(\frac{m_l c^2}{xT + Q}\right)^2}\, x^{2+j} f_l(x + Q/T) dx. \quad (57)$$

For easy of notation and consistency with the text, we note that $Q^{\rm CC}_{I,0} = R^{\rm CC}_I$, $Q^{\rm CC}_{I,1} = Q^{\rm CC}_I$, and $Q^{\rm CC}_{\nu_x,1} = Q^{\rm CC}_{\nu_x,0} = 0$.

In this case the neutrinos produce the phase-space blocking, thus in complete analogy to Eq. (41), we define

$$\langle 1 - f_I(\bar{E}_I)\rangle = \{1 + \exp[-(\bar{E}_I/T - \eta_I)]\}^{-1}, \quad (58)$$

such that the average energy of the produced neutrino $\bar{E}_I$ is given by

$$\bar{E}_I = \max\left[0, T\frac{\mathcal{I}^*_{I,1}}{\mathcal{I}^*_{I,0}} - Q\right]. \quad (59)$$

Similarly to the calculation of absorption opacities, we distinguish two cases:

(i) If $m_l c^2 - Q \le 0$, we set $x_{\min} = 0$ and compute the integral Eq. (57) with the modified lepton distribution function $f^*_l(x)$

$$f^*_l(x) = f_l(x + Q/T) = \frac{1}{1 + \exp(x - \eta^*_l)}, \quad (60)$$

$$\eta^*_l = \eta_l - \frac{Q}{T}, \quad (61)$$

which is the same integral as Eq. (43), up to a substitution $f_I(x) \to f^*_l(x)$.

(ii) If $m_l c^2 - Q > 0$, we make again $\epsilon + Q = E + m_l c^2$, $x = E/T$, which transforms the lepton distribution function and the lepton chemical potential, respectively, as

$$\tilde{f}^*_l(x) = \frac{1}{1 + \exp(x - \bar{\eta}^*_l)}, \quad (62)$$

$$\bar{\eta}^*_l = \eta_l - \frac{m_l c^2}{T}. \quad (63)$$

The resulting integral, then, is the same as Eq. (49), up to a substitution $\tilde{f}_I(x) \to \tilde{f}^*_l(x)$.

As per the pair processes, we follow the expressions of Ref. [60] for the electron-positron pair annihilation ($e^- e^+$) and transversal plasmon decay (γ) with a few adaptations, namely:

(i) For ν_x, we divide their Eqs. (B10), (B12) by 2 to account for our statistical weight 2 instead of 4.

(ii) For ν_μ and $\bar{\nu}_\mu$ produced via $e^- e^+$, we use their Eq. (B8), changing the term $(C_1 + C_2)_{\nu_e \bar{\nu}_e} \to (C_1 + C_2)_{\nu_x \bar{\nu}_x}$, and employ the degeneracies Eq. (18) to compute the corresponding blocking factors in their Eq. (B9).

(iii) Analogous adaptions were made in their Eqs. (B11), (B13) for the production of ν_μ and $\bar{\nu}_\mu$ via γ.

Then the free production rates in Eqs. (28), (29) are given by the sum of production rates over the charged-current and pair processes.

D. Limitations of the elastic approximation

Although in this work, we employ the elastic approximation for the computation of semileptonic neutrino opacities, in line with most of the work developed so far in the context of BNS merger simulations, it is important to point out that there is room for improvements in the modeling of weak neutrino interactions, for instance, the adoption of relativistic kinematics for nucleons [127], the inclusion of nuclear correlations in dense medium [128], or the full kinematics treatment [75]. In this section, we focus on comparing the opacities of charged-current processes obtained by Eq. (35) (employed in this work) with the full kinematics approach of Ref. [75], in which weak magnetism, pseudoscalar, and nuclear form factor are considered in a relativistic framework. Such a comparison was carried out in detail in Refs. [75,118,129] for conditions relevant to supernova matter, but here, we focus on conditions found in BNS merger remnants, summarized in Table II, where point A corresponds to the remnant core, point B to the hot,

TABLE II. Thermodynamic state of representative points extracted from our simulations. From left to right, the columns represent the point label, temperature, rest-mass density, proton fraction, muon fraction, neutron chemical potential, proton chemical potential, neutron-proton single particle interaction potential difference, neutron effective mass, proton effective mass, electron chemical potential, and muon chemical potential.

	T	ρ	Y_p	Y_μ	μ_n	μ_p	$U_n - U_p$	m^*_n	m^*_p	μ_e	μ_μ
Point	[MeV]	[g/cm^3]			[MeV]	[MeV]	[MeV]	[MeV]	[MeV]	[MeV]	[MeV]
A	10.0	1.2×10^{15}	0.08	0.025	1413	1192	7.6	349	347	209	192
B	30.0	5.0×10^{14}	0.06	0.015	1020	829	54.8	590	588	125	112
C	3.0	1.0×10^{10}	0.23	0	927	922	0.02	939	938	12.6	0

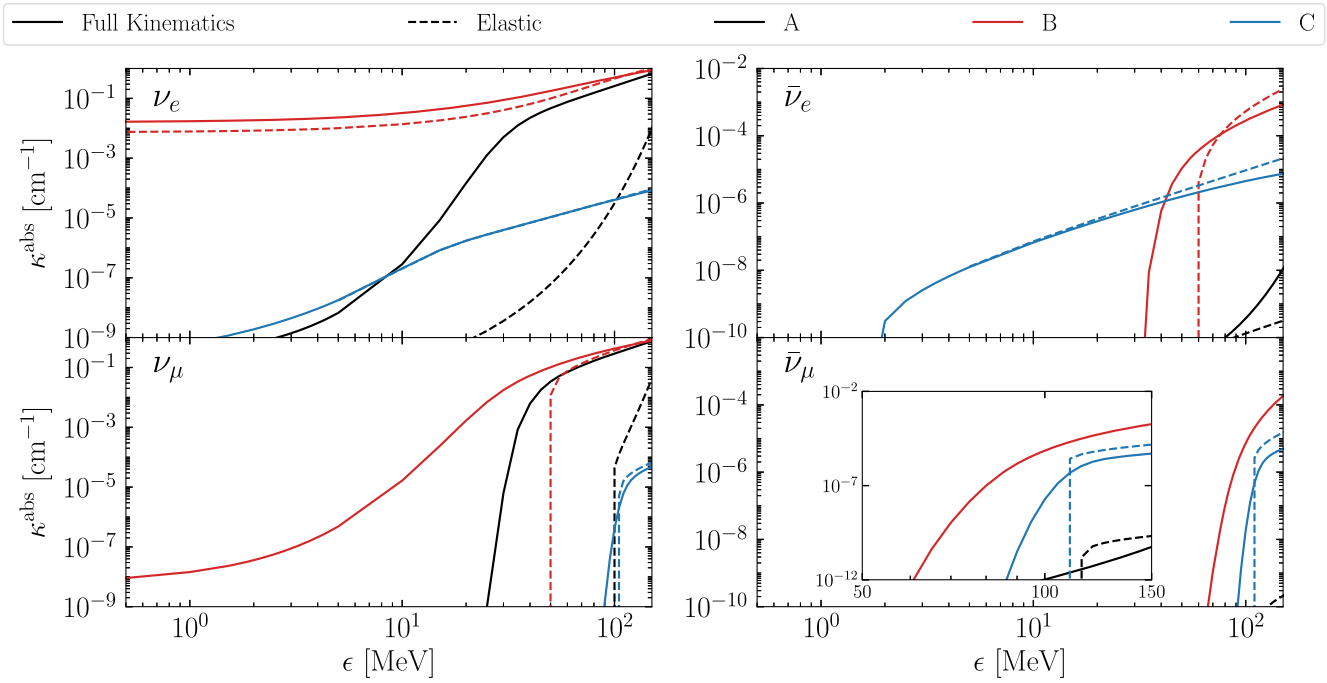


FIG. 3. Spectral absorption opacities for charged-current processes considered in this work in the full kinematics approach (solid lines) and in the elastic approximation (dashed lines) at relevant thermodynamical conditions A (black), B (red), and C (blue), representing the remnant core, hot interface and disk, respectively.

high-density interface between the core and the disk, and point C to the colder, low-density disk.

In Fig. 3, we show the spectral absorption opacity for each neutrino species in the full kinematics approach (solid lines) and in the elastic approximation (dashed lines) for each of the aforementioned thermodynamical points. First we note that the effects of the full kinematics treatment is more pronounced at high densities, where the momentum transfer becomes important (especially for $\nu_\mu, \bar{\nu}_\mu$ due to the high muon rest mass), as seen by the substantial opacity enhancement at points A and B across all neutrino species. The differences in opacity at point C (blue lines) are small for ν_e, ν_μ, but sizable for $\bar{\nu}_e$ ($\bar{\nu}_\mu$) at $\epsilon \geq 45$ MeV ($\epsilon \geq 90$ MeV) with up to an order of magnitude higher opacities in the elastic approximation. Muon (anti)neutrinos are expected to freely stream in this region, given that their average energy in equilibrium ($\langle \epsilon_{\nu_\mu,\bar{\nu}_\mu} \rangle = TF_3(\eta_{\nu_\mu,\bar{\nu}_\mu})/F_2(\eta_{\nu_\mu,\bar{\nu}_\mu}) \approx 10$ MeV) lies in the suppressed region.

In the remnant core (point A, black lines), we observe that ν_e absorption is greatly enhanced in the full kinematics approach at all neutrino energies, between several orders of magnitude for $\epsilon \leq 20$ MeV and 2 orders of magnitude at $\epsilon = 150$ MeV. The effect is more dramatic in the case of ν_μ, where the suppression threshold is reduced from $\epsilon = 98$ MeV to $\epsilon = 32$ MeV. Hence, the full kinematics approach should impact the neutrino trapping and thermalization in the core and consequently the conditions under which neutrinos of different energies decouple from matter [130]. Similar features are observed for $\bar{\nu}_e$ and $\bar{\nu}_\mu$, but given their small absorption opacities in this regime, it is expected that scattering will dominate the (fast) thermalization of antineutrinos, and no significant effect should arise from the full kinematics prescription.

In the hot core-disk interface (point B, red lines), we note that the absorption opacity for ν_e does not exhibit suppression at low energies and remains larger in the full kinematics approach by a factor of 1–2.5 for energies below 100 MeV, while for $\bar{\nu}_e$, the energy threshold decreases from ~55 MeV to ~32 MeV. The hard cutoff introduced by the elastic approximation at ~50 MeV (~160 MeV) for ν_μ ($\bar{\nu}_\mu$) is absent (relaxed to ~61 MeV) with the full kinematics treatment. Therefore, we expect that the substantial opacity increase across species could extend the neutrino spheres farther out of the remnant, leading to less effective neutrino cooling and less intense leptonization or deleptonization of the remnant, depending on the new positions of the neutrino spheres.

Here, we make a remark regarding the possible impacts of electron neutrino capture on nuclei A with N neutrons and Z protons,

$$\nu_e + A'(N+1, Z-1) \rightarrow A(N, Z) + e^-, \qquad (64)$$

which was not considered in the present work. Using the NuLib library [131], we computed the associated opacity based on weak rate tables of Refs. [132–135]. For the conditions A-C in Table II, the opacity is negligible due to the small fraction of nuclei. In fact, this reaction has

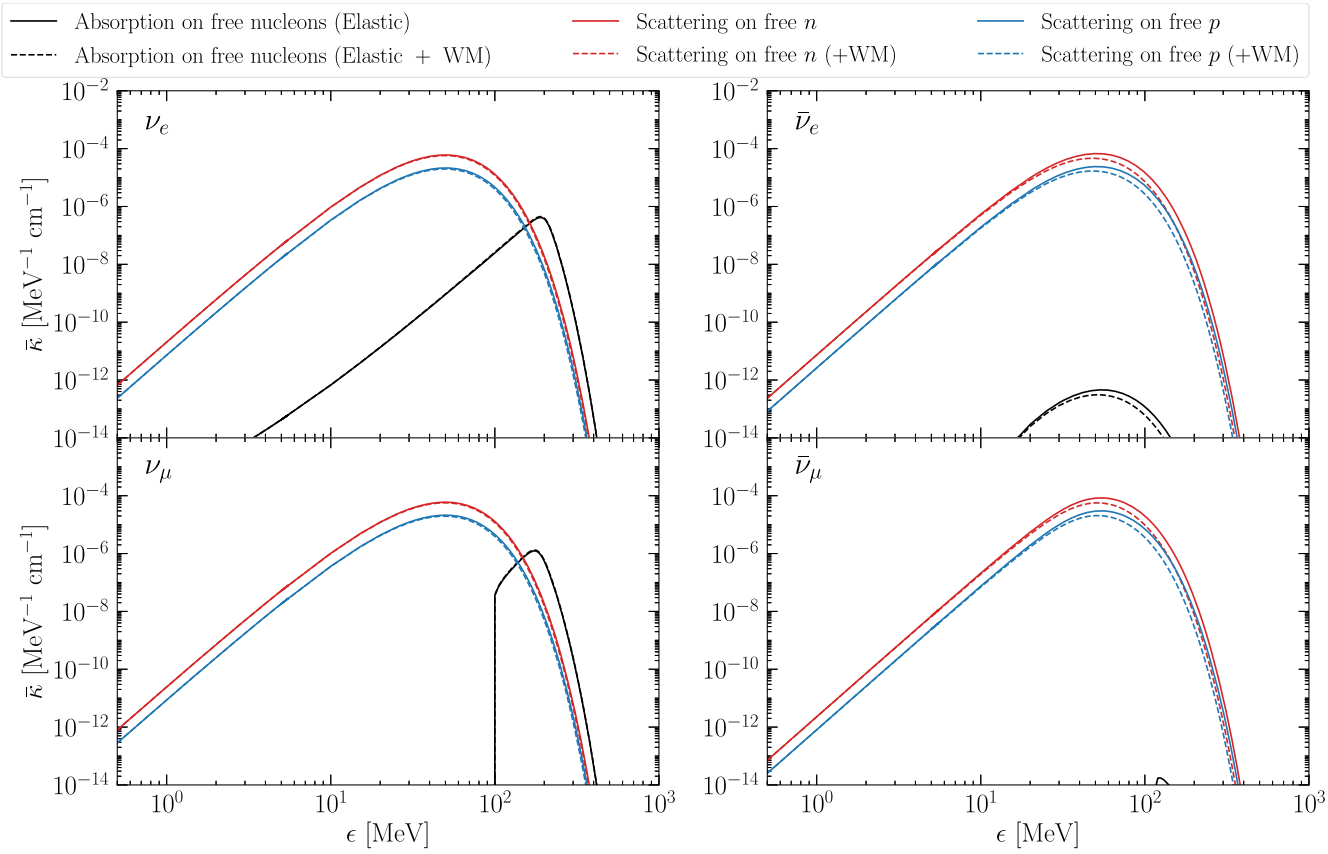


FIG. 4. Energy-weighted opacities for the weak reactions considered in this work in the elastic approximation (solid lines) and with weak magnetism/recoil corrections (dashed lines) at thermodynamical point A for electron neutrinos (upper left panel), electron antineutrinos (upper right panel), muon neutrinos (lower left panel), and muon antineutrinos (lower right panel). The lines represent absorption on free nucleons (black), scattering on free neutrons (red), and scattering on free protons (blue).

non-negligible opacity at ejecta conditions, i.e., densities $\rho \lesssim 10^{10}$ g/cm^3 and temperatures $T \lesssim 1$ MeV, but only at relatively large proton fraction $Y_p \gtrsim 0.4$. Due to the adoption of a leakage scheme, the later condition is never met in our simulations, as a full treatment of absorption seems to be necessary to produce highly protonized ejecta [136]. Hence, in scenarios where low density material is expected to become very proton rich, this reaction should not be ignored since it may dominate electron-neutrino capture on free neutrons.

As a last point, in the following, we investigate the impact of neglecting weak magnetism/recoil corrections (WM) in the form of multiplicative, energy-dependent factors, as proposed by Ref. [137]. To do so, we consider the same representative points of Table II and compute the energy-weighted opacities for the various neutrino species I

$$\bar{\kappa}_I(\epsilon) = \frac{\epsilon^3 f_I(\epsilon)}{T^4 F_3(\eta_I)} \kappa_I(\epsilon), \tag{65}$$

representing the quantity to be integrated in ϵ (up to average blocking factors) to produce the gray opacities employed in this work.

For the thermodynamical point A (core), we present in Fig. 4 the energy-weighted opacities. As anticipated, WM corrections are negligible for the reactions involving neutrinos (upper and lower left panels) but reduce opacities at higher neutrino energies for antineutrinos (upper and lower right panels). In particular, we note that under this thermodynamical condition, neutrinos are expected to be in thermal and weak equilibrium with the fluid. Given that in a gray scheme, the integral of the depicted quantity is the relevant quantity to be coupled to the fluid evolution and that the most noticeable effect is observed for iso-energetic elastic scattering on free nucleons for antineutrinos, WM contributes in reducing $\bar{\nu}_e$ and $\bar{\nu}_\mu$ opacities by a maximum ∼35%.

In Fig. 5, we repeat the analysis for thermodynamical point B (hot core-disk interface). Similarly, we note that WM corrections are small for neutrinos (upper and lower left panels) and most perceivable for iso-energetic elastic scattering on free nucleons. However, CC opacities dominate the integral by 1–2 orders of magnitude compared to scattering opacities, while WM contributes with a few percent deviation. There we note that WM corrections are once again small for the energy-integrated opacities of

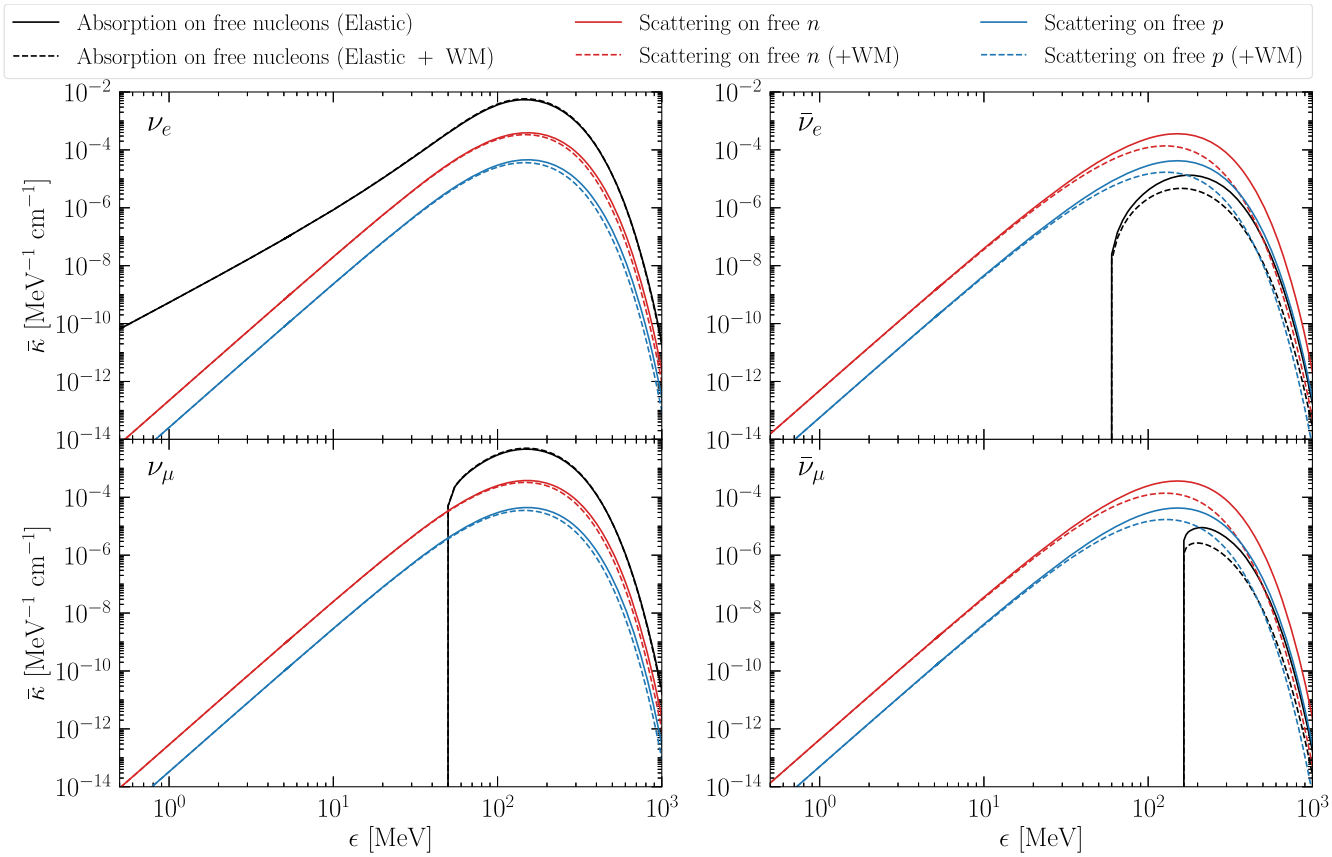


FIG. 5. Same as Fig. 4, but for thermodynamical point B, representing the hot core-disk interface.

neutrinos. On the other hand, WM corrections for antineutrinos (upper and lower right panels) noticeably decrease opacities at higher energies, but the weighting against the equilibrium distribution function for the computation of energy-integrated opacities limits this effect, as the antineutrino occupation number decreases. In this case, we see an overall reduction of ∼70% on energy-integrated opacities when WM corrections are included.

Hence, we have seen that WM corrections are responsible for significantly reducing opacities for antineutrinos across semileptonic CC and iso-energetic neutrino-nucleon elastic scattering reactions, in particular, for thermodynamical conditions where neutrinos should be trapped, thus where a slow diffusion ($t^{\rm diff} \gg t^{\rm prod}$) of thermalized neutrinos dominates the effective production rates [Eqs. (28) and (29)]. In this case, one expects very modest contributions of neutrino source terms to the fluid evolution.

In a leakage scheme, regions that are more strongly affected by neutrinos are usually located in the disk and polar cap, at optical depths from order of unit to order of tens, typically corresponding to $\rho = 10^{10}$–10^{12} g/cm^3 [130], where neutrinos decouple from matter and more energetic free emission contributes more to the effective rates. Thus, most of the impact of WM corrections in our simulations should come from thermodynamical conditions better represented by point C of Table II (outer disk), which coincides with matter conditions approximately at the $\bar{\nu}_e$ and $\bar{\nu}_\mu$ neutrino spheres, and points within the neutrino sphere with temperature $T \sim 1$–10 MeV and densities in the aforementioned range.

From Fig. 6, where outer disk conditions are represented, one notices negligible opacity deviations for neutrinos (on the percent level) and small deviations (on the few percent level) for antineutrinos. Considering that (i) the optical depth at a point is determined by the line integral of the opacity along a stationary path connecting the grid (or refinement level) boundary to said point and (ii) that WM corrections become less important away from the remnant, the positions of the neutrino spheres of all species should remain almost unaltered.

Therefore, one expects quantitative changes on simulation results by employing WM corrections with a leakage scheme prescription to be restricted to the region between the outer disk and the hot core-disk interface. In fact, for one such intermediate point (not shown), we observe reductions of ∼20–25% in the scattering and CC opacities of antineutrinos, suggesting impacts of the same order to the electronization of matter.

In summary, the matter dynamics within the core and the hot core-disk layer would be very slightly impacted due to

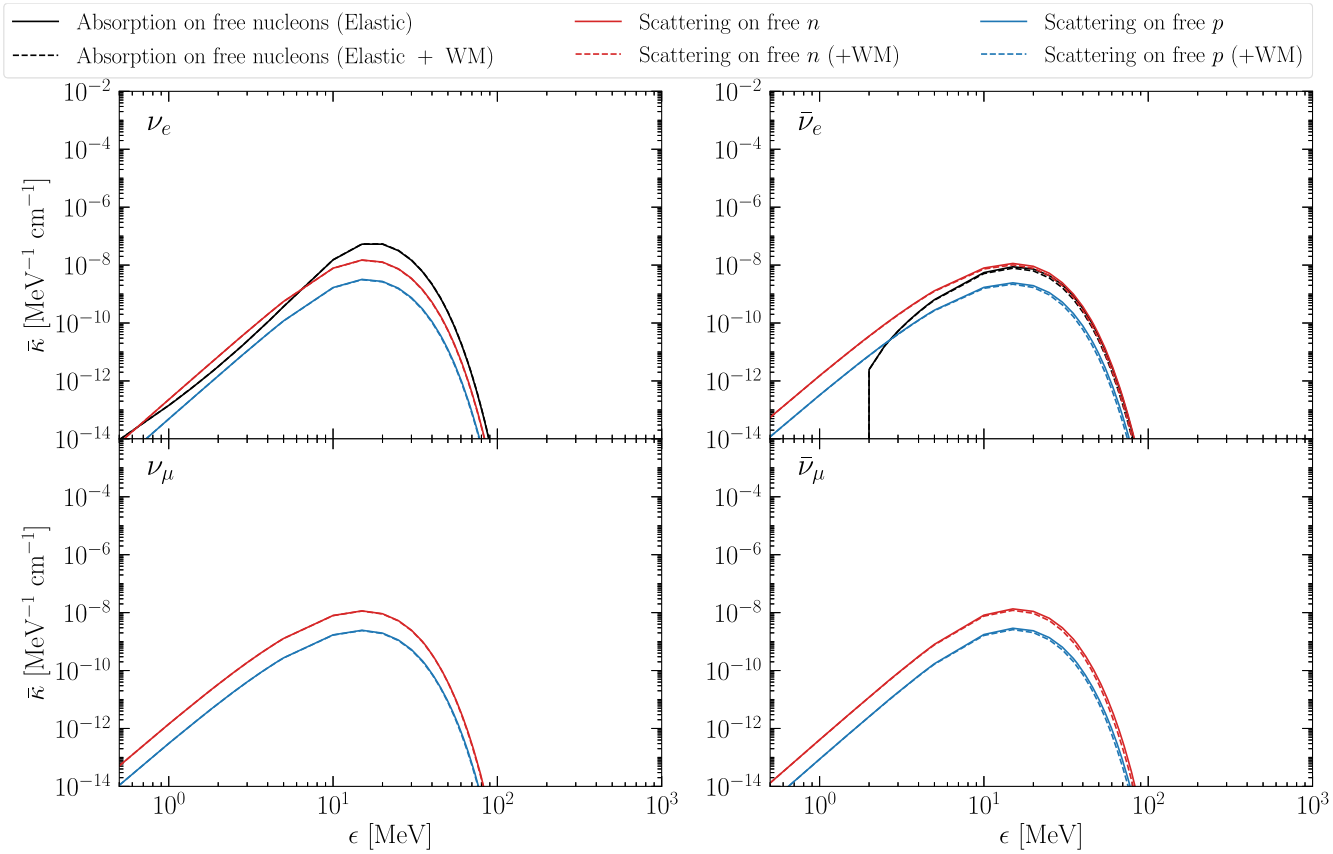


FIG. 6. Same as Fig. 4, but for thermodynamical point C, representing the outer disk.

the high optical depths found in such regions. Farther away from the outer disk and on the ejecta, the impacts should also be negligible, as density and temperature are significantly smaller.

It should be noted, however, that most of the differences expected to arise from the adoption of various treatments, either in the form of the full kinematics approach for charged-current processes or WM/recoil corrections to the elastic rates, would be better discernible with the adoption of a more advanced treatment for neutrinos transport, such as a moments scheme, given that neutrinos capture processes are the most affected by such corrections. With those limitations in mind, we present in the following the results obtained with the neutrinos leakage scheme and the elastic approximation for the charged-current opacities, suited for a first assessment of the impacts of muons and muonic weak reactions in BNS mergers.

IV. METHODS AND SETUPS

In this work, we performed four equal-mass, irrotational, BNS merger simulations. For our simulations, we employed the SFHo baseline EOS. For comparison purposes, we ran one simulation with electrons and positrons only, which corresponds to a three-dimensional EOS, incorporating the usual three neutrino species $\{\nu_e, \bar{\nu}_e, \nu_x\}$, $\nu_x = \nu_\mu, \bar{\nu}_\mu, \nu_\tau, \bar{\nu}_\tau$, with $g_{\nu_x} = 4$. This setup is referred to as SFHo_3D. The other three setups were simulated with the full four-dimensional EOS. In order to single out the role of muons-driven reactions, one of the four-dimensional EOS setup was simulated with the same aforementioned three neutrino species, hence named SFHo_4D_3, while the remaining two were simulated with five neutrino species $\{\nu_e, \bar{\nu}_e, \nu_\mu, \bar{\nu}_\mu, \nu_x\}$, $\nu_x = \nu_\tau, \bar{\nu}_\tau$, $g_{\nu_x} = 2$, identified as SFHo_4D_5, with same spatial grid resolution as the previously described runs, and SFHo_4D_5_High, with higher spatial grid resolution. All systems have total gravitational mass $M = 2.70 M_\odot$ and are initially governed by cold $T = 0.1$ MeV, neutrinoless β-equilibrated EOSs. The initial data was produced with the SGRID code [138–140], adapted to the use of one-dimensional tabulated EOSs as input. One caveat is that finite-temperature EOSs hardly reproduce the limit $(p, \varepsilon) \to 0$ for $n_b \to 0$, which is needed for the proper imposition of boundary conditions. Instead, there is typically a (small) critical density n_b^* for which $de/dn_b|_{n_b^*} = 0$ and such that $de/dn_b > 0$ for $n_b < n_b^*$ [141]. To ensure the desired behavior at densities below the critical one, we assume that in this region, the EOS is described by a cold polytrope.

The dynamical evolution of the spacetime and matter was performed with the BAM code, which received the

updates described in Sec. II and in Sec. III. The numerical domain consists in a hierarchy of 7 nested Cartesian grids (referred to as levels and indexed by $L \geq 0$) with $\Delta x_L/\Delta x_{L+1} = 2$ grid spacing refinement. For $L \geq 3$, the levels move following the motion of the stars.

The finest level ($L = 6$) has grid spacing $\Delta x_6 = 178$ m and $\Delta x_6 = 142$ m for the high resolution run. The space is discretized with fourth-order finite differencing, while all fields evolve in time using the method of lines with an explicit fourth-order Runge-Kutta integrator and the Berger-Oliger time stepper [142]. Geometry quantities are evolved with the Z4c formulation of Einstein's equations [143,144] along with the moving punctures method [87,145]. Gauge fields are evolved adopting the $1 + \log$ slicing [146] and the Gamma-driver conditions [147]. The HRSC scheme adopted for the evolution of matter fields employs the WENOZ reconstruction [148] and the HLL Riemann solver [149,150] for the computation of intercell fluxes. Finally, a conservative adaptative mesh refinement strategy is used to ensure mass conservation across refinement levels [47]. The low density regions outside of the stars are treated with an artificial atmosphere prescription according to which matter elements are static and the thermodynamical properties follow from a cold and β-equilibrated slice of the EOS.

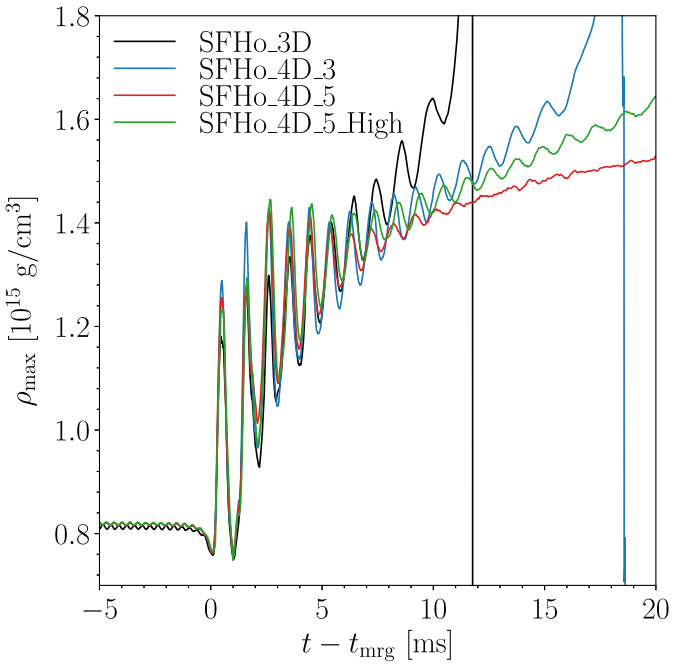


FIG. 7. Maximum rest-mass density evolution for our simulated setups. The merger instant $t_{\rm mrg}$ is defined as the instant in which the amplitude of the dominant (2,2) mode of the GW strain is maximum.

V. MERGER AND POSTMERGER DYNAMICS

A. Matter evolution

All simulations begin with a coordinate distance between stars ≈41.4 km, merging after ∼4 orbits. As expected, the presence of muons and muon-driven neutrino reactions does not affect the orbital dynamics during the inspiral.

In Fig. 7, we depict the time evolution of the maximum rest-mass density $\rho_{\max}$ for our simulated setups. We begin noting that the muonic EOSs exhibit a slightly larger maximum rest-mass density before the merger, which is a consequence of the slightly smaller internal energy at same density introduced by the inclusion of muons in the cold, β-equilibrated EOSs employed for the construction of the ID.

In good agreement with the results from Ref. [70], our SFHo_3D simulation collapsed to a black hole in ∼12 ms after the merger, which, despite important differences between the hydrodynamics and NLS implementations, is reassuring. Next, we note that the SFHo_4D_3 run has its collapse delayed by ∼7 ms compared to SFHo_3D, which suggests a stabilizing role of the muons in the densest portions of the remnant with a noticeable damping of $\rho_{\max}$ oscillations until the collapse. Furthermore, the remnant of the five-species run SFHo_4D_5 experiences a stronger damping of the oscillations and does not collapse within our simulation time span. It is worth pointing out that gravitational collapses are rather sensitive to grid resolution; thus, the observation of a longer-lived remnant in SFHo_4D_5_High, albeit exhibiting weaker damping as the oscillations are sustained for longer, suggests that the stabilization is robust.

For a more complete description of the reported stabilization, it is useful to introduce the reduced gravitational binding energy E_b and reduced angular momentum $j_{\rm red}$, defined as [136,151]

$$E_b = \frac{1}{\mu M}(M_{\rm ADM} - E_{\rm GW} - M), \tag{66}$$

$$j_{\rm red} = \frac{1}{\mu M^2}(J_{\rm ADM} - J_{\rm GW}), \tag{67}$$

where $M_{\rm ADM}$ ($J_{\rm ADM}$) is the ADM mass (angular momentum) of the system at the initial time slice, $M = M_1 + M_2$ is the total gravitational mass, $E_{\rm GW}$ ($J_{\rm GW}$) is the energy (angular momentum) radiated by GWs (see Ref. [151] for the definitions of $E_{\rm GW}$ and $J_{\rm GW}$), and $\mu = M_1 M_2/(M_1 + M_2)^2$ is the symmetric mass ratio. For our simulations, $M_{\rm ADM} = 2.672 M_\odot$, $M = 2.7 M_\odot$, $J_{\rm ADM} = 7.064 M_\odot^2$, and $\mu = 1/4$. Physically, E_b characterizes the compactness of the system, while $j_{\rm red}$ represents its angular momentum.

As depicted in Fig. 8, the time evolution of $-E_b$ (thick lines) and $j_{\rm red}$ (dashed lines) agree until the merger for all runs. Up to 5 ms after the collision, the muonic runs emit more energy in the form of GWs, following the larger central density oscillations. Within this time span, the

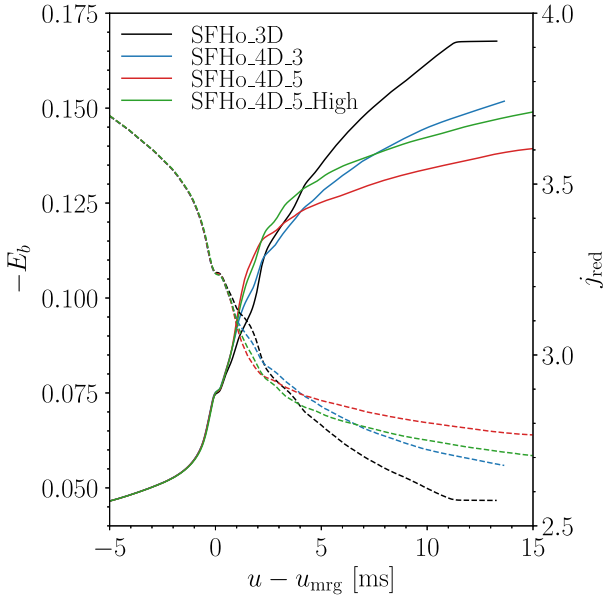


FIG. 8. Evolution of the gravitational binding energy $-E_b$ (thick lines) and reduced angular momentum $j_{\rm red}$ (dashed lines) for our simulated setups. GW contributions to both quantities are extracted at a sphere of constant coordinate radius $r = 1000M_\odot$. We employ the retarded time u to account for the time of flight of the signal to the extraction sphere.

muonic systems are more compact, as expected from the softening of the EOS in the presence of muons, and SFHo_4D_5 is more compact than SFHo_4D_3 because some muonization occurs between the fusing cores (more details in Sec. V C). Hence, the muonic setups undergo a more violent merger event. In this early stage, the evolution at high densities is dominated by GW emission; thus, the energetics of neutrino emission is of little dynamical importance. At 5 ms, the remnant cores reach approximately the same central density, and we note the formation of a trend in $-E_b$, namely that SFHo_3D, is more strongly bound than SFHo_4D_3, which is more strongly bound than SFHo_4D_5. On the other hand, the ordering is reversed for $j_{\rm red}$ and for the retained mass within the remnants of each setup, suggesting that a stronger bounce efficiently distributes mass and angular momentum outward. Accordingly, density oscillations are weakened, which in turn, reduces energy and angular momentum losses via GWs. The remnant becomes less bound (higher $-E_b$), and a stronger rotational support (higher $j_{\rm red}$) prevents further contraction of the remnant. Indeed, the residual angular momentum of SFHo_4D_5 is enough to stabilize the remnant (at least up to our final simulation time), while for SFHo_4D_3, the smaller $j_{\rm red}$ only delays the collapse. At increased grid resolution, we note that the remnant is more strongly bound, and rotational support is weaker for SFHo_4D_5_High, leading to the longer-sustained oscillations and larger central rest-mass density when compared to SFHo_4D_5.

Now we proceed with an analysis of the remnant and disk structure. In Fig. 9, we depict the matter state on the x-y plane 10 ms after the merger. First we note that the SFHo_3D setup develops the most compact disk (upper row, first column), with a hot core-disk interface, pronounced shocked-tidal arms (middle row, first column) and a highly protonized disk, with $Y_p \gtrsim 0.25$ up to 40 km from the origin (lower row, first column). The SFHo_4D_3 run (second column) exhibits more pronounced tidally shocked arms, although with overall smaller temperatures throughout the remnant core and disk, leading to a less protonized disk. It is worth noticing that the higher proton fraction in the densest portions of the muonic runs is reminiscent from the more protonized initial data (see Fig. 1).

The five-species runs SFHo_4D_5 and SFHo_4D_5_High (third and fourth columns) develop an extended $\rho \geq 10^{13}$ g/cm^3 region, with a noticeable suppression of the formation of tidally shocked arms. Accordingly, the whole remnant and disk are cooler than for SFHo_4D_3 and SFHo_3D, and the proton fractions are smaller (lower row, third and fourth columns). In fact, weaker protonization is a direct consequence of the inclusion of muonic reactions since the additional cooling by emission of muon-flavored neutrinos leads to a reduced electronization of matter via emission of electron-flavored neutrinos (a full presentation and discussion of neutrino luminosities are found in the next section).

Complementary to the snapshots presented in Fig. 9, we show in Fig. 10 the time evolution of mass-averaged quantities of interest in the orbital plane.

We begin noting that the average temperature (upper panel) is overall higher for the SFHo_3D run along the postmerger, which follows from a less potent neutrino cooling (see the luminosities presented in the next section). Even with the same set of weak reactions, SFHo_4D_3 is colder due to an increase of ∼10% of the specific heat capacity at constant pressure under relevant conditions when muons are included. This increase is somewhat expected, given the enhanced energy cost of heating up a matter element containing one additional (massive) leptonic species. Furthermore, we verified that this increase is dominated by leptonic contributions because changes in the baryonic contribution to the heat capacity due to the increased proton fraction in the presence of muons are very modest. In addition to that, in the SFHo_4D_5 run, we observe that cooling provided by muonic weak reactions contributes to lowering the average temperatures and to the suppression of temperature oscillations at later times. Finally, the higher average temperature observed in the SFHo_4D_5_High run is a resolution effect, related to a better capture of shocks during the postmerger.

In the following, we present a brief discussion about the evolution of the average muon fraction (middle panel), while in Sec. V C, we present in more details the relevant microphysics that determines the muonic content found in

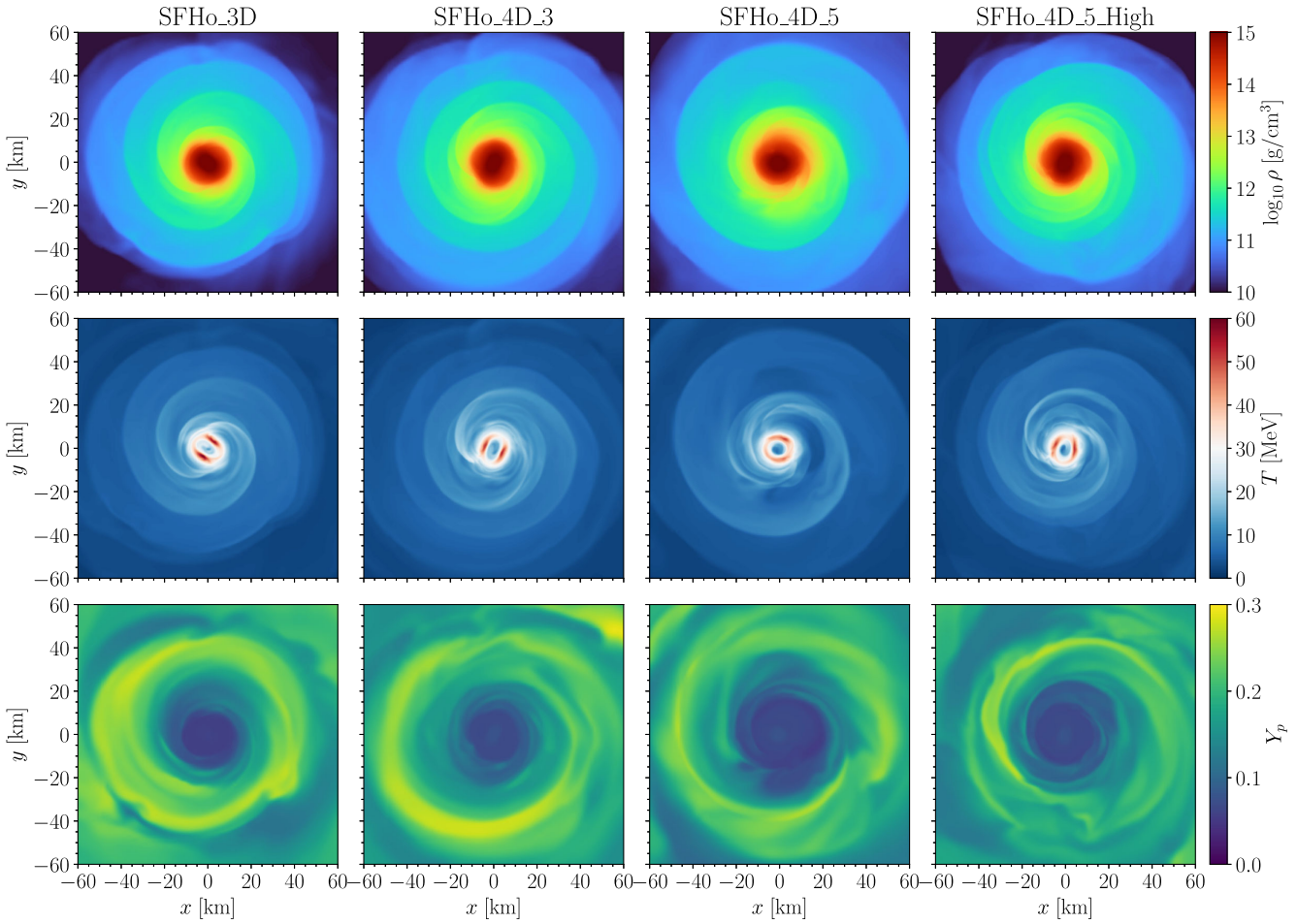


FIG. 9. Matter properties in the $x-y$ plane for the SFHo runs at $t-t_{\rm mrg}=10$ ms. Columns are referred from left to right as first to fourth. *First column:* SFHo_3D. *Second column:* SFHo_4D_3. *Third column:* SFHo_4D_5. *Fourth column:* SFHo_4D_5_High. *Upper row:* rest-mass density. *Middle row:* temperature. *Lower row:* proton fraction.

our simulations. In the SFHo_4D_3 run, we observe peaks (up to 2 ms after the merger) with approximately the same $\langle Y_\mu\rangle \sim 0.0215$, associated to the oscillations of the remnant. Since in this run there are no CC muonic reactions, the total number of muons is conserved, and the subsequent decrease is set by the advection of muons from the core toward the disk. When CC muonic reactions are taken into account, as seen for SFHo_4D_5(_High), the peaks become more pronounced, indicating episodes of alternating muonization and demuonization. Then, at later times, the average muon fraction decreases substantially as a consequence of demuonization of intermediate-low density material. It is worth pointing out that the smaller value for SFHo_4D_5 compared to SFHo_4D_3 before the merger results from demuonization already at the inspiral stage, being the same effect at play during the late time demuonization.

Finally, the average proton fraction (bottom panel) increases along the postmerger for SFHo_3D, which is expected from the very well known electronization of matter under postmerger conditions. For the muonic runs, the average proton fraction is larger, as set by the initial data, having similarities with the evolution of the average muon fraction due to local charge neutrality, most notable in the first 2 ms of the postmerger. At later times, we observe a steady increase in response to the electronization of matter, with a slower growth for SFHo_4D_5(_High).

We end this section by remarking that the remnant structures of the muonic runs, e.g., extended remnant and disks, are fully consistent with our analysis in terms of binding energy and angular momentum. Future work employing different EOSs will be necessary to understand whether the observed stabilization via rotational support is general.

B. Neutrino emission

In Fig. 11, we present the evolution of the neutrinos source luminosities. The pronounced peaks in the upper panels are associated to the gravitational collapse. Overall we note that the emissions peak around ∼2 ms for all setups. The higher total luminosity peak of SFHo_4D_3

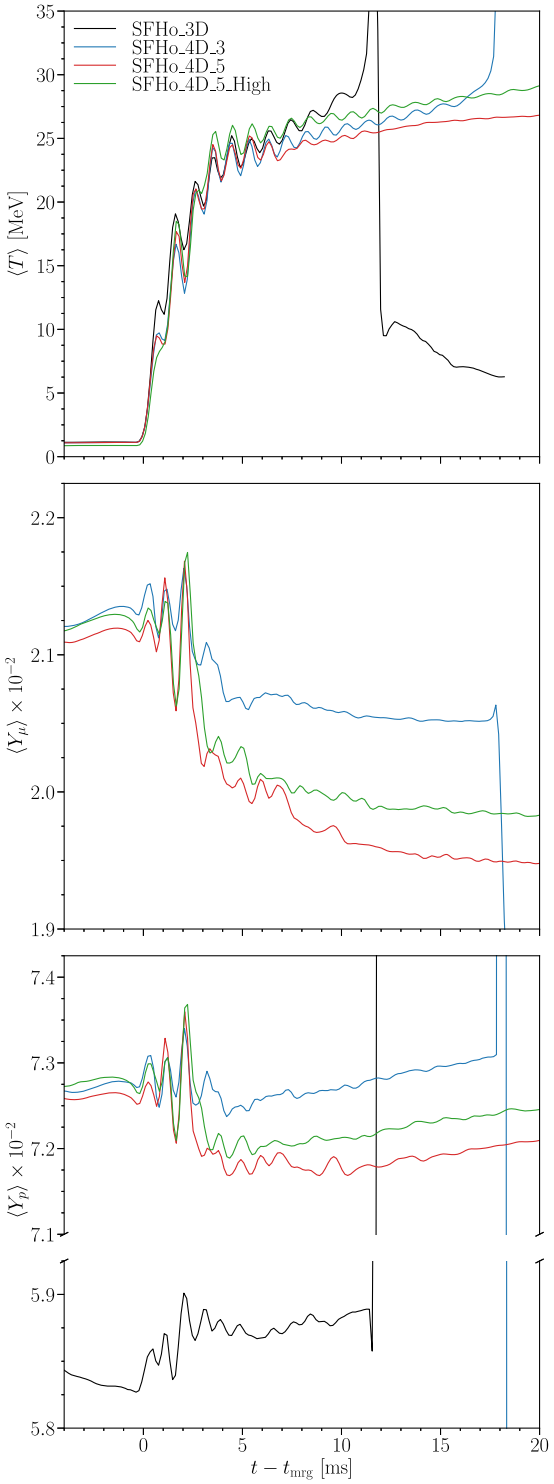


FIG. 10. Evolution of the mass-averaged matter properties on the $x-y$ plane. Quantities are shown as moving time averages with window 0.5 ms. *Upper panel:* average temperature, where we note that three-species run reaches overall higher temperatures compared to the muonic runs at the same grid resolution. *Middle panel:* average muon fraction for the muonic runs. *Bottom panel:* average proton fraction, where the higher values achieved during the inspiral by the muonic runs are reminiscent from the more protonized cores in the initial data.

(upper right panel) when compared to the SFHo_3D (upper left panel) at this instant follows from the higher $\rho_{\max}$ reached by the former (see Fig. 7). In this case, the compression of matter increases the reaction rates across all neutrinos species.

Along the postmerger stage, $\bar{\nu}_e$ dominates up to 6 ms, followed by ν_x for the three-species runs SFHo_3D and SFHo_4D_3. After that, L_{ν_x} is otherwise comparable to $L_{\bar{\nu}_e}$ because of the high temperatures reached by the remnants and the strong temperature scaling of pair processes yielding ν_x. Note that for the five-species simulations, L_{ν_x} is smaller than in the three-species counterparts, because in the latter, ν_x represents the four species $\{\nu_\mu, \bar{\nu}_\mu, \nu_\tau, \bar{\nu}_\tau\}$, and hence the effective rates contain statistical weight 4, while in the former, ν_x represents $\{\nu_\tau, \bar{\nu}_\tau\}$ with statistical weight 2 (see Sec. IV). Direct comparison shows that $L_{\nu_\mu} + L_{\bar{\nu}_\mu} + L_{\nu_x} > L_{\nu_x}^{3-\text{species}}$, which suggests that the additional cooling provided by muonic β processes in the five-species scenario removes thermal energy from the fluid that would power the emission of heavy-lepton neutrinos via pair processes. This same effect leads to the overall smaller luminosities observed across all neutrino species. It is worth pointing out that during the formation of a black hole, we do not adopt any particular excision strategy. Instead, we let the rest-mass density evolve and linearly extrapolate thermodynamical quantities for densities above the maximum tabulated one. Such a procedure is somewhat arbitrary, but since this only happens within the apparent horizon (hence causally disconnected from the remaining of the grid), no significant effect is observed in the matter properties outside of the apparent horizon. However, since the optical depths computation depends on neighboring points, which might include points within the apparent horizon, unphysical optical depths may develop as a consequence of the linear extrapolation of opacities in those regimes. This is what we observe after the collapse for SFHo_4D_3: The maximum rest-mass density reaches between two and three times the maximum tabulated value, which produces unphysically high opacities and, consequently, very high optical depths within the apparent horizon. The optical depths at neighboring points then increase in response, leading to very small effective emission rates Eqs. (28), (29) and source luminosities. Contrary, for the SFHo_3D run, the maximum rest-mass density within the apparent horizon is ∼50% larger than the maximum tabulated value; thus, the opacities do not reach as high of values, and the optical depths are not contaminated by the region within the apparent horizon. Therefore, we are able to capture the fading luminosity emitted by the disk. For the five-species runs SFHo_4D_5 (lower left panel) and SFHo_4D_5_High (lower right panel), we observe an overall larger total luminosity, which we associate to the additional cooling channels provided by the CC muonic reactions. The early postmerger neutrinos burst is such that the luminosities for ν_e, ν_μ, and $\bar{\nu}_\mu$ are

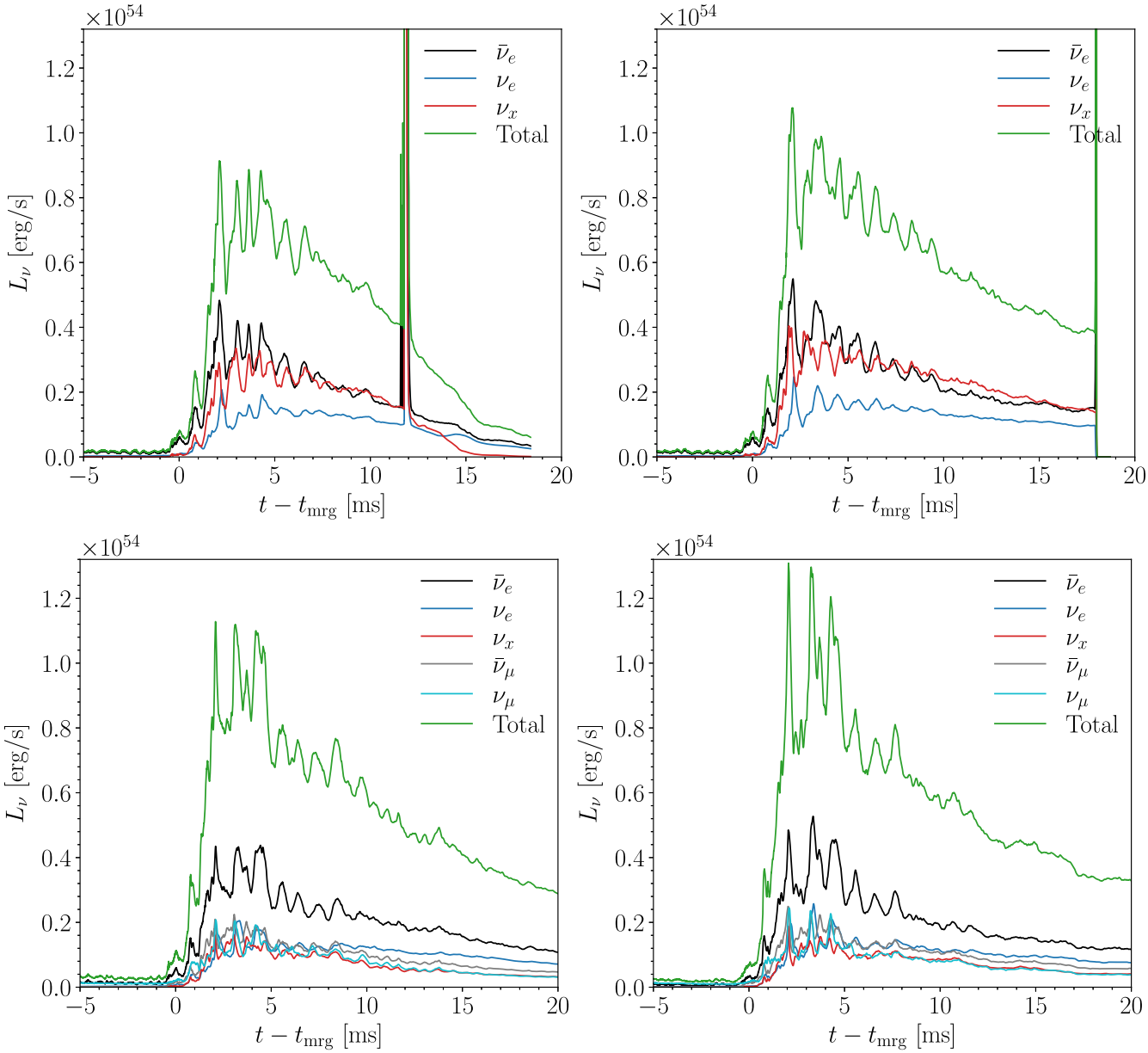


FIG. 11. Source neutrino luminosity L_ν evolution. *Upper left panel:* SFHo_3D, where the peak around 12 ms is related to the gravitational collapse. *Upper right panel:* SFHo_4D_3, where we followed the simulation up to 1 ms after the collapse for the purpose of comparing the remnant evolution with the remaining setups. *Lower left panel:* SFHo_4D_5. *Lower right panel:* SFHo_4D_5_High. In all setups, we note a burst of neutrinos shortly after the merger, prompted by the heating that follows the compression of matter elements. Before the merger, neutrinos are produced due to artificial heating produced by shocks in the interface between the stars and the atmosphere, although to a lesser degree with increased grid resolution.

comparable up to ∼5 ms. Once the emissions stabilize (from around 10 ms on), $L_{\nu_\mu} < L_{\bar{\nu}_\mu}$ because the hot and dense remnant is essentially optically thick and neutrinos mostly diffuse with average energies $\langle E_{\bar{\nu}_\mu} \rangle > \langle E_{\nu_\mu} \rangle$, as suggested by the average neutrino energies presented in Table III. We note that here the average neutrino energy is estimated as the ratio between energy and particle source luminosities, defined as in Ref. [96], thus based on volume integrals over a grid level and without gravitational redshift corrections. Naturally, our reported average energies are higher by ∼50% for all species when compared to the literature (e.g., Refs. [68,71,72,113]), which is an expected feature for leakage schemes given that neutrino luminosity and energy estimates include neutrinos in the hot and dense remnant. On the other hand, more advanced treatments include absorption, and neutrino properties are extracted far from the remnant, hence, in the freely streaming regime. Additionally, it is important to note that neutrino-electron scattering (NES) might play an important

TABLE III. Average neutrino energy per species, in MeV, 10 ms after the merger for our simulated setups. The columns read simulation name, average electron neutrino energy, average antielectron neutrino energy, average muon neutrino energy, average antimuon neutrino energy, and average heavy lepton-neutrino energy.

Simulation	$\langle E_{\nu_e}\rangle$	$\langle E_{\bar{\nu}_e}\rangle$	$\langle E_{\nu_\mu}\rangle$	$\langle E_{\bar{\nu}_\mu}\rangle$	$\langle E_{\nu_x}\rangle$
SFHo_3D	15.3	22.2	⋯	⋯	34.8
SFHo_4D_3	15.8	21.5	⋯	⋯	33.7
SFHo_4D_5	15.0	21.5	29.4	44.1	34.0
SFHo_4D_5_High	15.2	22.0	28.6	40.3	34.1

role for the thermalization of muon and tau-flavored neutrinos (see, e.g., [152]). If included, one expects smaller $\langle E_{\nu_\mu}\rangle$, $\langle E_{\bar{\nu}_\mu}\rangle$, and $\langle E_{\nu_x}\rangle$ due to loss of neutrino energy in such inherently inelastic processes. Therefore, considering our simplified approach, our estimates should be regarded as semiquantitative.

Nevertheless, for all cases, we recover the usual hierarchy $\langle E_{\nu_x}\rangle > \langle E_{\bar{\nu}_e}\rangle > \langle E_{\nu_e}\rangle$. Irrespective to the presence of muons and muonic weak reactions, $\langle E_{\nu_e}\rangle$, $\langle E_{\bar{\nu}_e}\rangle$, and $\langle E_{\nu_x}\rangle$ agree within ∼5%. Interestingly, for the five-species runs, we note that ∼10 ms after the merger, the neutrino spheres for $\bar{\nu}_\mu$, ν_x, and ν_μ are, respectively, located at increasing radii from the remnant center, although somewhat close, and are found deeper within the remnant, hence at higher matter temperatures, than the $\bar{\nu}_e$ and ν_e neutrino spheres. Thus, our results are in qualitative agreement with the conclusion of Ref. [113] that the observed energy hierarchy is related to the higher temperature of the medium from which ν_x, ν_μ, and $\bar{\nu}_\mu$ decouple, with a caveat that there the authors employ an M0 scheme for the transport of energy and particle number, hence approximately accounting for neutrino absorption. Besides, since the emission rates for pair processes are the same for ν_μ and $\bar{\nu}_\mu$, their difference in average energies comes from the CC reactions. In fact, by enforcing the lower bound on the energy of neutrinos that may be emitted via CC processes, we have $E_{\bar{\nu}_\mu,\min} = m_\mu c^2 + Q \approx 107$–$170$ MeV, while $E_{\nu_\mu,\min} = m_\mu c^2 - Q \approx 45$–$104$ MeV. Our results suggest the following neutrino energy hierarchy: $\langle E_{\bar{\nu}_\mu}\rangle > \langle E_{\nu_x}\rangle > \langle E_{\nu_\mu}\rangle > \langle E_{\bar{\nu}_e}\rangle > \langle E_{\nu_e}\rangle$, although further simulations employing more EOSs and an improved neutrino treatment are desirable to draw firmer conclusions.

C. Muon content

In order to describe the evolution of the muonic content, we introduce the conserved muon number, defined as

$$m_b N_\mu = \int_{\mathcal{V}} D Y_\mu \sqrt{\gamma} d^3x, \tag{68}$$

where $D = W\rho$ is the rest-mass density in the Eulerian frame, W is the usual Lorentz factor, and the integration volume $\mathcal{V}$ is a grid level. In the absence of muonic weak reactions, the balance-law Eq. (23) implies the approximate constancy of N_μ along the evolution, which is verified for SFHo_4D_3 up to the collapse in the upper panel of Fig. 12. In contrast, when CC muonic reactions are included [SFHo_4D_5(_High) runs], we observe that the conserved muon number decreases by as much as 8% (4%) with respect to the initial condition within our simulation time span. In fact, we observe an early demuonization, prompted by the expansion of cold, low density material into the artificial atmosphere (more details in the following). However, such an effect is diminished both before and after the merger with increased grid resolution because the hydrodynamics is better resolved and less matter expands into the atmosphere.

The demuonization can be visualized in the lower panels of Fig 12, where we show Y_μ in the $x-y$ plane 10 ms after the merger. For the SFHo_4D_3 run (lower left panel), we note that a substantial $Y_\mu > 0.01$ is distributed throughout the disk, which is a hydrodynamical effect attributed to the sourceless advection of muons from the remnant core. Contrary, for the SFHo_4D_5 (lower middle panel) and SFHo_4D_5_High (lower right panel), muons are found only within the remnant, where $\rho \geq 10^{14}$ g cm^{-3} (see third and fourth, left panels of Fig. 9), rapidly decreasing outside of this region, as indicated by the $Y_\mu = 10^{-6}$ red dashed contour line.

For a better understanding of the conditions in which (de)muonization operates, we present in Fig. 13 the effective muon production rate $\mathcal{R}_{Y_\mu}$

$$\mathcal{R}_{Y_\mu} = \frac{\alpha m_b}{W\rho}(R^{\rm eff}_{\bar{\nu}_\mu} - R^{\rm eff}_{\nu_\mu}), \tag{69}$$

which is simply the rhs of Eq. (23) combined with the baryon number conservation Eq. (24) and represents the time rate of change of Y_μ by the emission of muon-flavored neutrinos. Hence, $\mathcal{R}_{Y_\mu} > 0$ (red colorbar) corresponds to muonization, $\mathcal{R}_{Y_\mu} < 0$ (blue colorbar) corresponds to demuonization, and white regions correspond to negligible production rates. It is clear that muonization is more intense in the hot, medium-density, shocked regions, represented by the point marked with a circle, where $\mathcal{R}_{Y_\mu} > 10^{-2}$/ms and $\rho = 2.7 \times 10^{12}$ g/cm^3, $T = 21.4$ MeV, $Y_p = 0.14$, and $Y_\mu = 0.024$. On the other hand, in the innermost portions of the remnant, where densities are higher, muonization proceeds much more slowly (10^{-3}–10^{-6}/ms), allowing a modest muon buildup in the shear heated region between the fusing cores. Furthermore, the slower observed muonization confirms the findings of Ref. [85], that the bulk of muons found in the interior of the remnant at later times are reminiscent from the initial cold cores.

In contrast, demuonization is observed predominantly in cold, medium-to-low density matter streams. The

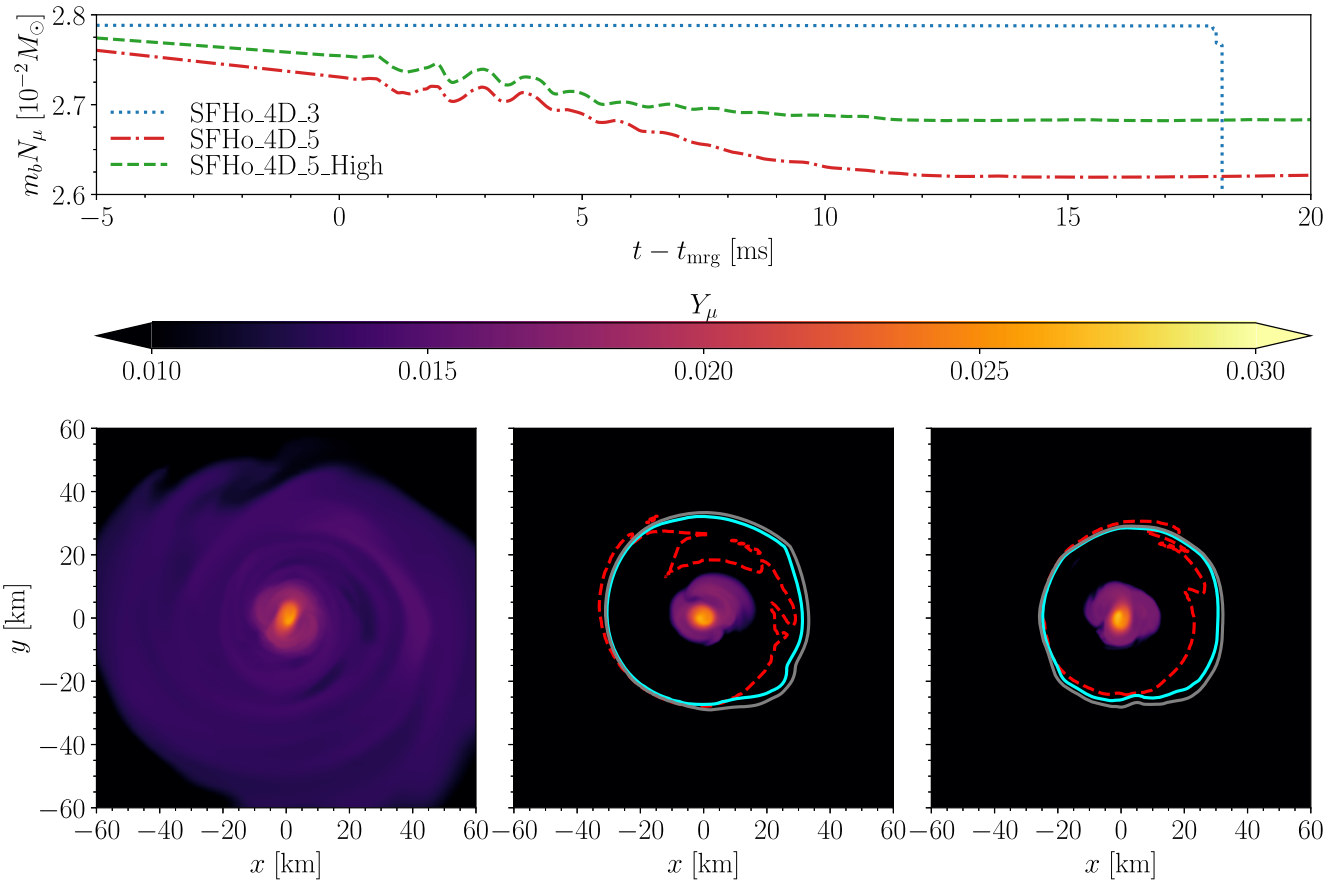


FIG. 12. Evolution of the muon fraction for the muonic SFHo runs. *Upper panel:* Evolution of the conserved number of muons in the grid level $L = 1$. The three-species run SFHo_4D_3 conserves $m_b N_\mu$ along the evolution, while the five-species exhibits demuonization of matter. Here, we observe that such effect takes place before the merger due to the expansion of low density, cold material into the atmosphere, but to lesser extent with increased resolution. *Lower panels:* Y_μ on the $x - y$ plane 10 ms after the merger. *Lower left panel:* SFHo_4D_3 run, where the region with $Y_\mu > 0.01$ extends up to 60 km from the origin. *Lower middle panel:* SFHo_4D_5 run, where the disk is found demuonized, while $Y_\mu \gtrsim 0.015$ is present in regions where $\rho \geq 10^{14}$ g cm^{-3}. *Lower right panel:* SFHo_4D_5_High run. The red dashed line marks $Y_\mu = 10^{-6}$ and the thick contour lines mark the neutrino spheres of ν_μ (cyan) and $\bar{\nu}_\mu$ (gray), where $\tau_{\nu_\mu,0} = \tau_{\bar{\nu}_\mu,0} = 1$.

square marker in Fig. 13 represents a point where $|\mathcal{R}_{Y_\mu}| > 10^{-2}$/ms, $\rho = 4.8 \times 10^{11}$ g/cm^3, $T = 6.8$ MeV, $Y_p = 0.16$, and $Y_\mu = 1.63 \times 10^{-6}$. Therefore, during the remnant's evolution, it is expected that matter elements in the outermost regions will decompress and cool, eventually reaching thermodynamic conditions where demuonization operates fast.

In order to have a qualitative understanding of the thermodynamics of demuonization, we present in Fig. 14 the muon fraction in neutrinoless β-equilibrium $Y_\mu^{\rm eq}$ (blue to red colorbar), obtained by solving Eqs. (9), (14) over the whole EOS subspace (ρ, T). We stress out that the neutrinoless hypothesis is not particularly accurate at high densities since neutrinos are expected to be in the trapped regime [93], but it is a suitable approximation to model the equilibration in a low-density environment, where neutrinos should be freely streaming.

The diagram encodes most of the relevant information regarding the β-equilibration process for muons, which we highlight in the following. First, at low temperatures, muons are present only at sufficiently high densities, e.g., where $\mu_e \geq m_\mu c^2$. At densities smaller than $\approx 1.8 \times 10^{14}$ g/cm^3 and temperatures smaller than ≈ 10 MeV, the equilibrium fractions are negligible, but at higher temperatures, $Y_\mu^{\rm eq}$ rapidly increases as the muon/antimuon gas becomes non-degenerate. In the purple-green colorbar, we present the deviation of the muon fraction Y_μ in the $x - y$ plane at $t - t_{\rm mrg} = 1.6$ ms with respect to the β-equilibrium value at the densities and temperatures encountered in our simulation. There it becomes clear that cold ($T \leq 10$ MeV) matter elements with $\rho \leq 10^{12}$ g/cm^3, corresponding to the typical thermodynamical conditions where higher demuonization rates are observed in Fig. 13, are not only effectively demuonized, but also that such demuonization is a

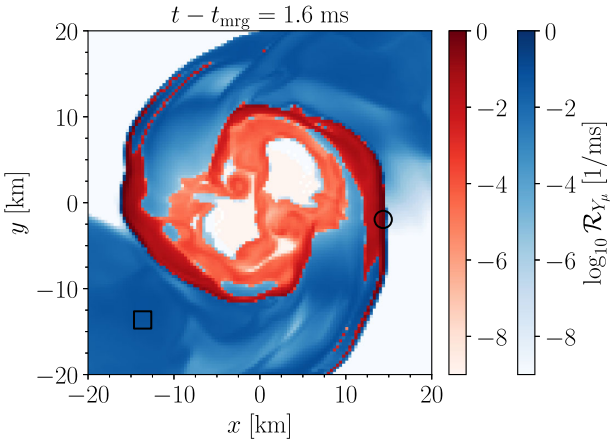


FIG. 13. Effective muon production rate due to emission of muon-flavored neutrinos for the SFHo_4D_5 run at $t - t_{\rm mrg} = 1.6$ ms, roughly coinciding with the increase in $m_b N_\mu$ depicted in the upper panel of Fig. 12. The red colorbar represents regions where $\mathcal{R}_{Y_\mu} > 0$ (muonization), while the blue colorbar represents regions where $\mathcal{R}_{Y_\mu} < 0$ (demuonization). For reference, we mark with a black circle a point with high muonization rate, and a square marks high demuonization rate.

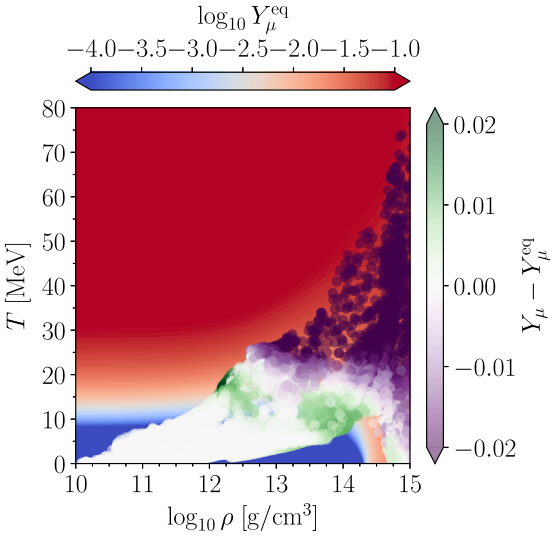


FIG. 14. Neutrinoless β-equilibrium values $Y_\mu^{\rm eq}$ of the muon fraction with respect to (ρ, T) (blue-red colorbar) and deviation $Y_\mu - Y_\mu^{\rm eq}$ of simulated Y_μ with respect to equilibrium (purple-green colorbar). In the diagram, we see that at temperatures $T \lesssim 15$ MeV and low densities, simulated values are found in equilibrium, marked by white points. Out-of-equilibrium matter elements are expected to equilibrate either by demuonization (green points), found at intermediate densities and temperatures, or muonization (purple points), located at $T \gtrsim 15$ MeV.

consequence of β equilibration. This phenomenology plausibly explains the early demuonization during the inspiral.

Green points represent matter elements with muon fraction in excess, hence expected to demuonize, and are predominantly distributed in a region 10^{12} g/cm$^3 \leq \rho \leq 2 \times 10^{14}$ g/cm^3 and temperatures smaller than 20 MeV.

Purple points represent matter elements expected to muonize, mainly found at temperatures higher than 20 MeV and to a lesser extent at densities $\approx 10^{15}$ g/cm^3. Those points are mapped to positive production rates (see Fig. 13), but since most of the muonization occurs very slowly, at $\mathcal{R}_{Y_\mu} < 10^{-4}$/ms (except for the shocked arms), the faster decompression, cooling and subsequent demuonization dominate the muon fraction evolution up to the stationary state depicted in the upper panel of Fig. 12.

Here, we make some remarks about our findings. First, the muon fraction distributions along the x-y plane at $t - t_{\rm mrg} = 5$ ms are similar to Fig. 3 of Ref. [85]; i.e., around the final instants of the neutrino bursts, we found $Y_\mu = 10^{-4}$–10^{-2} within 25 km of the recently formed remnant for the five-species runs, which is due to the early redistribution of Y_μ from the merging cores. Thus, the demuonization reported by us operates on longer timescales, mostly affecting the outermost disk regions.

Next, it is worth pointing out that, contrary to the CCSNe simulations of Refs. [74,76], we do not observe the muonization of high-density matter, which is explainable by the following: First, their simulations start without muons within the matter. Then a substantial Y_μ builds up only shortly before the core bounce and after it, most importantly through a two-stages process comprised of production of high-energy muon-(anti)neutrinos via pair processes that may then participate in muonic absorption reactions. Such a mechanism cannot be properly modeled by a neutrinos leakage scheme because absorption is not realistically captured by the treatment. Second, the protonization observed in NLS simulations is based on an excess emission of $\bar{\nu}_e$ with respect to ν_e, which occurs in the intermediate region between spatially separated $\bar{\nu}_e$ and ν_e neutrino spheres such that $\tau_{\bar{\nu}_e,0} = 1$ is located closer to the remnant than $\tau_{\nu_e,0} = 1$. This is not the case for ν_μ and $\bar{\nu}_\mu$ neutrino spheres. Instead, what we observe is that the $\bar{\nu}_\mu$ neutrino sphere is slightly wider than the ν_μ neutrino sphere, as depicted in the lower panels of Fig. 12. This happens because the spectrally averaged opacities employed in this work are heavily dominated by scattering processes in the muon (anti)neutrino neutrino spheres. Besides, there the neutrino degeneracies are relatively small $\eta_{\nu_\mu} = -\eta_{\bar{\nu}_\mu} \approx -2$, such that the number-averaged opacity is typically a few tens of percent larger for $\bar{\nu}_\mu$ than for ν_μ. On the other hand, the maximum values of the optical depths found during the postmerger are around one order of magnitude smaller for $\bar{\nu}_\mu$ than for ν_μ, which is expected given that the energy-dependent CC opacities are 1 to 2 orders of magnitude smaller for $\bar{\nu}_\mu$ than for ν_μ under remnant and disk conditions [76]. Compared to late stages of the postbounce reported by Ref. [76], we found Y_μ in excess of about 1 order of magnitude. This is because most

TABLE IV. Ejecta properties for our simulated setups. Columns show the simulation, ejecta mass extracted at $r = 200M_\odot$, ejecta mass extracted at $r = 300M_\odot$, average proton fraction, average entropy per baryon, and average velocity measured by an observer at infinity. All average quantities were extracted at $r = 300M_\odot$. For the muonic runs, $\langle Y_\mu \rangle \lesssim 10^{-3}$, and thus $\langle Y_p \rangle \approx \langle Y_e \rangle$.

	$M_{\rm ej}^{r=200M_\odot}$	$M_{\rm ej}^{r=300M_\odot}$	$\langle Y_p \rangle$	$\langle s \rangle$	v_∞
Simulation	$[10^{-3}M_\odot]$	$[10^{-3}M_\odot]$		$[k_B]$	$[c]$
SFHo_3D	2.8	2.2	0.17	11.3	0.19
SFHo_4D_3	1.9	1.2	0.20	12.0	0.17
SFHo_4D_5	1.5	1.0	0.16	11.4	0.16
SFHo_4D_5_High	1.6	1.0	0.19	13.6	0.14

of the Y_μ found in the remnant cores come from the initially cold, neutrinoless, β-equilibrated NSs, while in the former, matter is still hot ($T \approx 15$ MeV) and far from β equilibrium, i.e., there $\mu_n - \mu_p < \mu_\mu < \mu_e$. Finally, our Y_μ values are comparable to Ref. [74] under similar thermodynamic conditions, which also agree with the reported in Refs. [85,86].

VI. EJECTA ANALYSIS

In this section, we present an analysis of the ejecta properties for our simulations. The relevant quantities are summarized in Table IV. We note that the geodesic criterion [153] was adopted, and the reported averages were extracted at a fixed sphere of coordinate radius $r = 300M_\odot$ by the procedure outlined in Ref. [72].

We begin comparing our SFHo_3D results with works that employ similar physical setups and neutrinos treatment. Our ejecta masses extracted at $r = 200M_\odot$ are, respectively, ≈30%(≈23%) smaller than those in Ref. [66] (Ref. [65]). When comparing ejecta masses extracted at $r = 300M_\odot$ with those of Ref. [70], we have ≈37% less. Such differences may be partly explained by differences in the hydrodynamics implementations; e.g., Refs. [66,70] employ a positivity-preserving limiter with the MP5 reconstruction and a different prescription for the atmosphere [51]. On the other hand, our approach for the computation of opacities and emissivities should also contribute, given that ejecta properties are importantly impacted by the treatment of neutrinos.

Regarding average properties, good agreement is found for $\langle Y_p \rangle$, although our $\langle s \rangle$ is smaller by ∼24%, and v_∞ is smaller by ∼27% compared to Ref. [70].

Comparing our SFHo runs, the SFHo_4D_3 setup has a more protonized $\langle Y_p \rangle = 0.20$ and slightly more entropic $\langle s \rangle = 12.0$ ejecta than SFHo_3D, although less massive by a factor 1.5–1.8. The smaller amount of ejecta is consistent with the larger total luminosity of the former compared to the later (see Fig. 11), by means of which energetic matter elements become gravitationally bound due to neutrinos emission. The same rationale applies to the SFHo_4D_5 and SFHo_4D_5_High setups, which exhibit even higher total luminosities because of the additional muonic charged-current cooling channels. It should be noted, however, that our interpretation does not rule out the possibility that pressure changes due to the presence of muons may also affect the ejecta mass, as pointed out in Ref. [85].

At same grid resolution, SFHo_3D and SFHo_4D_5 have very similar $\langle Y_p \rangle$ and $\langle s \rangle$, with differences mainly in v_∞ by a factor of ∼1.2 and in ejecta masses by a factor of 1.9–2.2. With increasing resolution, we note that SFHo_4D_5 and SFHo_4D_5_High vary by less than 10% in the ejecta masses and in less than 20% in $\langle Y_p \rangle$, $\langle s \rangle$ and v_∞, allowing us to estimate numerical uncertainties of at least 20%.

In Fig. 15, we present the distributions of ejected mass fractions with respect to the proton fraction Y_p (left panel), entropy per baryon s (middle panel), and asymptotic velocity v_∞ (right panel) for our simulations, extracted

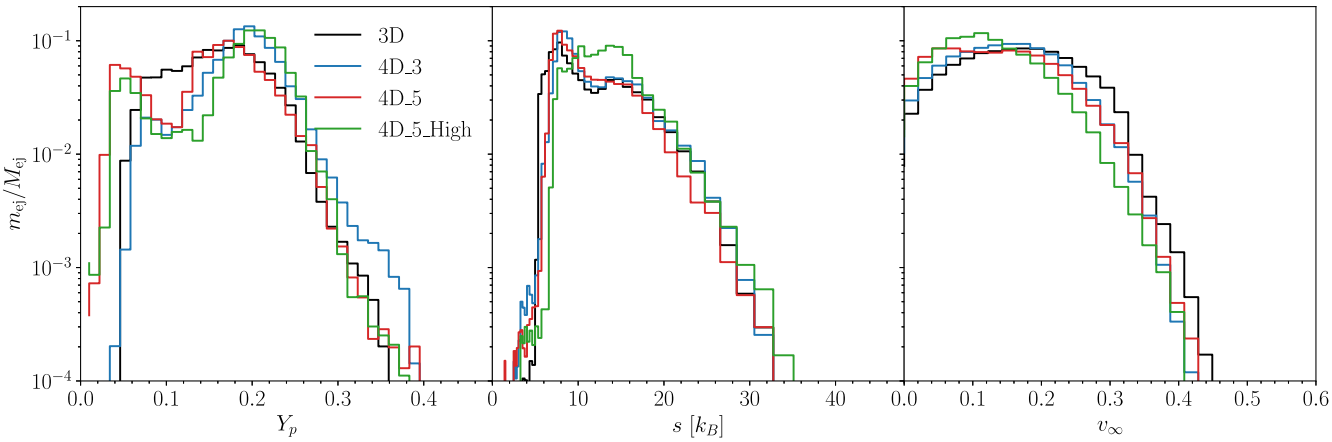


FIG. 15. Distribution of ejecta mass detected at $r = 300M_\odot$ with respect to the proton fraction Y_p (left panel), entropy per baryon (middle panel), and asymptotic velocity (right panel).

at $r = 300M_\odot$. Since at this position, the muon fraction Y_μ for the muonic runs are much smaller than Y_p, the distributions are identical with respect to Y_e, and our results may be compared to others from the literature. Comparing our SFHo_3D result (left panel) to similar runs of Refs. [66,70], our Y_p distribution is flatter from $Y_p = 0.06$ up to the peak at $Y_p = 0.20$, followed by a similar falloff for $Y_p \geq 0.3$. For SFHo_4D_3, the distribution is more clearly peaked at $Y_p = 0.20$, with a considerably smaller fraction of neutron-rich material and a tail of neutron-poor material $Y_p \leq 0.30$. We verified that, in both simulations, the (neutron-rich) tidal component of the ejecta is rapidly reached by the (neutron-poor) shock-driven component of the ejecta, such that the material is reprocessed and the distribution is shifted toward higher Y_p values. In the case of SFHo_4D_5 and SFHo_4D_5_High runs, the additional energy and momentum losses associated to the muonic reactions yield higher fractions of small velocity material (see right panel of Fig. 15). Hence, the reprocessing mechanism is inhibited, and we note a pronounced neutron-rich secondary peak along with the expected dominant neutron-poor peak. It should be noted that the higher peak around $Y_p = 0.2$, and the prolonged tail found for the muonic runs follows from the longer simulation times until collapse. Hence, matter with higher proton fraction have sufficient time to travel to the extraction sphere. The entropy per baryon distribution (middle panel) is very similar across all setups at same grid resolution peaking at $s \sim 8k_B$ and followed by a rapid decay such that a negligible fraction of the ejecta is found with $s \geq 32k_B$. For the SFHo_4D_5_High setup, the peak is shifted toward $s \sim 14k_B$ and a tail is found up to $s \sim 35k_B$. The asymptotic velocity (right panel) follows a similar pattern for all simulations with a trend that increased amounts of small velocity ejecta are found in runs with higher total neutrinos luminosities. Besides, we did not find in our simulations a fast ejecta component as reported in Ref. [70].

VII. CONCLUSIONS

In this work, we presented, for the first time, a set of binary neutron star merger simulations that include muons and muonic weak reactions. To do so, we introduced a scheme to produce four-dimensonal EOS tables parametrized by (ρ, T, Y_p, Y_μ) by "dressing" a three-dimensional baryonic baseline EOS with a leptonic EOS modeling electrons, positrons, muons, and antimuons as relativistic, ideal Fermi gases.

Next, we introduced a scheme for the tabulation of neutrinos opacities and emission rates that, differently from previous works [60,105] in which most of the BNS studies are based on, here we included in-medium corrections embodied by the medium-modified Q factor for the charged-current absorption and emission reactions, as in Refs. [75,76,118,121], but we restricted our treatment to the elastic approximation. In future works, it would be important to consider the full kinematics approach of Ref. [75,76] since it implies important corrections to the neutrinos opacities.

We ran a set of BNS simulations adopting the SFHo baseline baryonic EOS, modeling neutrinos as per a leakage scheme incorporating the aforementioned updated sets of neutrinos opacities and emission rates. For comparison purposes, our SFHo_3D setup was simulated with a three-dimensional EOS including electrons and positrons and the usual three-species $\{\nu_e, \bar{\nu}_e, \nu_x\}$. For this particular setup, we observed gravitational collapse, in good agreement with Ref. [70], with smaller ejecta masses by a few tens of percent compared to Refs. [65,66,70]. At this stage, it is difficult to point out to which extent those differences arise due to different hydrodynamics implementations and to neutrinos treatment. We also ran three simulations including muons, namely SFHo_4D_3, SFHo_4D_5, and SFHo_4D_5_High, the first one with three-neutrino species and the remaining with five-neutrino species $\{\nu_e, \bar{\nu}_e, \nu_\mu, \bar{\nu}_\mu, \nu_x\}$, explicitly separating the muon-flavored neutrinos $\nu_\mu, \bar{\nu}_\mu$ from the heavy-lepton neutrinos ν_x and adopting charged-current muonic reactions. The last setup has increased grid resolution with respect to the remaining ones. For SFHo_4D_3, the collapse was delayed by $\sim$7 ms, while for SFHo_4D_5, there is no collapse within our simulation time (up to 20 ms after the merger), and we note a significant damping of the central rest-mass density oscillations. At increased resolution, SFHo_4D_5_High also does not collapse within 20 ms. We found that the stabilization is provided by increased rotational support. In fact, the softening of the high-density EOS by inclusion of muons leads to a more violent merger event, followed by a stronger centrifugal bounce. This effect is more pronounced for SFHo_4D_5(_High) since some muonization in the early postmerger allows the densest regions of the remnant to retain higher Y_μ compared to SFHo_4D_3, for which Y_μ is simply advected outward into the disk. The centrifugal bounce redistributes matter and angular momentum such that the remnant for the muonic runs become less compact and, thus, more stable against gravitational collapse.

Regarding the evolution of the muon content along the postmerger stage, we note that when muonic CC reactions are neglected, and Y_μ is advected from the remnant core, distributing $Y_\mu > 0.01$ relatively far within the disk. When muonic CC reactions are included, the disk is found effectively demuonized, as expected by the β equilibration of lower density, cold material and $Y_\mu > 0.01$ is restricted to dense portions of the remnant with $\rho \geq 10^{14}$ g/cm^3.

In order to stress out the limitations of our methods, we presented a comparison between opacities obtained with the elastic approximation and the full kinematics approach for selected thermodynamical conditions found in our

simulations, concluding that, in general, weak rates in the elastic approximation are underestimated by factors that range between a few and orders of magnitude, depending on the neutrino energy. The difference between approaches is, as expected, more evident at higher densities, where the matter dynamics is less sensitive to details of the neutrino transport scheme. Such a comparison can also be seen in, e.g., Ref. [118].

At small densities ($\rho \leq 10^{10}$ g/cm^3) and small temperatures, found in the disk and polar regions, elastic and full kinematics approaches produce almost the same CC rates. Besides, since the opacities there are very small for (anti) muon neutrinos, whose average energies in equilibrium lie in the strongly suppressed region, one does not expect absorption to significantly modify the muonic content. Therefore, we believe that a more realistic neutrino transport treatment should not qualitatively alter the demuonization scenario presented here, given that it is an expected outcome of β equilibration in the freely streaming regime.

We expect, however, that the adoption of a neutrino transport with proper absorption treatment, combined with full kinematics rates, would affect the early postmerger, where temperatures larger than $T = 15$ MeV enable sizable absorption of ν_μ, which in turn allows those hot spots to retain muons and impact the dynamics of the system by softening the EOS. Additionally, higher-energy (anti)muon neutrinos emitted at higher temperatures could be reabsorbed in optically thinner regions, possibly reducing the demuonization rates.

For the muonic simulations, we found systematically smaller amounts of ejecta compared to SFHo_3D. This is consistent with the reported higher total neutrino luminosities, which indicate that energy is effectively drawn from outflowing matter elements, preventing them from escaping the system. Structurewise, the muonic simulations exhibit less compact and cooler disks. In particular, we noted that the inclusion of muonic CC reactions leads to the suppression of the formation of shocked arms along the disk. Furthermore, despite the initially higher proton fraction in the interior of NSs containing muons, which is retained throughout the postmerger stage, the disk is less protonized than in the nonmuonic counterpart. Overall our results suggest that the inclusion of muons and muonic weak reactions leads to significant consequences regarding the outcomes of BNS merger simulations, mostly affecting the postmerger evolution, the thermal and compositional structure of the remnant and, consequently, the ejecta properties. In future works, we plan on extending the M1 scheme of Ref. [72] to account for muon-flavored neutrinos interactions and simulate a number of different baseline baryonic EOSs in order to assess the impacts of a more realistic neutrinos treatment. Finally, it is important to point out that, at typical BNS remnant temperatures and densities, a sizeable population of pions is expected to be present [154]. In this case, the equilibrium composition of a NS is altered by the increase in the proton content, which leads to a softening of the EOS. Consequently, macroscopic properties of a NS are significantly altered by the inclusion of pions [86,155], as well as BNS merger simulations outcomes, e.g., postmerger GW frequencies, threshold binary mass for prompt gravitational collapse, and ejecta properties. Furthermore, weak interaction reactions involving pions and muons may be an important source of opacity for low-energy muon-flavored neutrinos. Hence, we also intend to extend our formalism in the future to investigate to the role pions and muons in BNS merger simulations.

ACKNOWLEDGMENTS

H. G., F. S., and T. D. acknowledge funding from the EU Horizon under ERC Starting Grant No. SMArt-101076369. The simulations were performed on HPE Apollo Hawk at the High Performance Computing (HPC) Center Stuttgart (HLRS) under the Grant No. GWanalysis/44189, on the GCS Supercomputer SuperMUC-NG at the Leibniz Supercomputing Centre (LRZ) [Project No. pn29ba], and on the HPC systems Lise/Emmy of the North German Supercomputing Alliance (HLRN) [Project No. bbp00049].

DATA AVAILABILITY

The data that support the findings of this article are not publicly available upon publication because it is not technically feasible and/or the cost of preparing, depositing, and hosting the data would be prohibitive within the terms of this research project. The data are available from the authors upon reasonable request.

[1] B. P. Abbott *et al.* (Virgo and LIGO Scientific Collaborations), Phys. Rev. Lett. **119**, 161101 (2017).
[2] J. Aasi *et al.* (LIGO Scientific Collaboration), Classical Quantum Gravity **32**, 074001 (2015).
[3] F. Acernese *et al.* (VIRGO Collaboration), Classical Quantum Gravity **32**, 024001 (2015).
[4] A. Hajela *et al.*, Astrophys. J. Lett. **886**, L17 (2019).
[5] A. Hajela *et al.*, Astrophys. J. Lett. **927**, L17 (2022).
[6] A. Balasubramanian, A. Corsi, K. P. Mooley, K. Hotokezaka, D. L. Kaplan, D. A. Frail, G. Hallinan, D. Lazzati, and E. J. Murphy, Astrophys. J. **938**, 12 (2022).

[7] V. Nedora, T. Dietrich, M. Shibata, M. Pohl, and L. C. Menegazzi, Mon. Not. R. Astron. Soc. **520**, 2727 (2023).
[8] H. Wang, R. G. Dastidar, D. Giannios, and P. C. Duffell, Astrophys. J. Suppl. Ser. **273**, 17 (2024).
[9] V. Savchenko *et al.*, Astrophys. J. Lett. **848**, L15 (2017).
[10] B. P. Abbott *et al.* (LIGO Scientific, Virgo, Fermi-GBM, and INTEGRAL Collaborations), Astrophys. J. Lett. **848**, L13 (2017).
[11] B. P. Abbott *et al.* (LIGO Scientific, Virgo, Fermi GBM, INTEGRAL, IceCube, AstroSat Cadmium Zinc Telluride Imager Team, IPN, Insight-Hxmt, ANTARES, Swift, AGILE Team, 1M2H Team, Dark Energy Camera GW-EM, DES, DLT40, GRAWITA, Fermi-LAT, ATCA, ASKAP, Las Cumbres Observatory Group, OzGrav, DWF (Deeper Wider Faster Program), AST3, CAASTRO, VINROUGE, MASTER, J-GEM, GROWTH, JAGWAR, CaltechNRAO, TTU-NRAO, NuSTAR, Pan-STARRS, MAXI Team, TZAC Consortium, KU, Nordic Optical Telescope, ePESSTO, GROND, Texas Tech University, SALT Group, TOROS, BOOTES, MWA, CALET, IKI-GW Follow-up, H.E.S.S., LOFAR, LWA, HAWC, Pierre Auger, ALMA, Euro VLBI Team, Pi of Sky, Chandra Team at McGill University, DFN, ATLAS Telescopes, High Time Resolution Universe Survey, RIMAS, RATIR, and SKA South Africa/MeerKAT Collaborations), Astrophys. J. Lett. **848**, L12 (2017).
[12] I. Arcavi *et al.*, Nature (London) **551**, 64 (2017).
[13] D. A. Coulter *et al.*, Science **358**, 1556 (2017).
[14] V. M. Lipunov *et al.*, Astrophys. J. Lett. **850**, L1 (2017).
[15] N. R. Tanvir *et al.*, Astrophys. J. **848**, L27 (2017).
[16] S. Valenti, D. J. Sand, S. Yang, E. Cappellaro, L. Tartaglia, A. Corsi, S. W. Jha, D. E. Reichart, J. Haislip, and V. Kouprianov, Astrophys. J. **848**, L24 (2017).
[17] E. Annala, T. Gorda, A. Kurkela, and A. Vuorinen, Phys. Rev. Lett. **120**, 172703 (2018).
[18] A. Bauswein, O. Just, H.-T. Janka, and N. Stergioulas, Astrophys. J. **850**, L34 (2017).
[19] F. J. Fattoyev, J. Piekarewicz, and C. J. Horowitz, Phys. Rev. Lett. **120**, 172702 (2018).
[20] M. Ruiz, S. L. Shapiro, and A. Tsokaros, Phys. Rev. D **97**, 021501 (2018).
[21] M. Shibata, S. Fujibayashi, K. Hotokezaka, K. Kiuchi, K. Kyutoku, Y. Sekiguchi, and M. Tanaka, Phys. Rev. D **96**, 123012 (2017).
[22] D. Radice, A. Perego, F. Zappa, and S. Bernuzzi, Astrophys. J. **852**, L29 (2018).
[23] E. R. Most, L. R. Weih, L. Rezzolla, and J. Schaffner-Bielich, Phys. Rev. Lett. **120**, 261103 (2018).
[24] I. Tews, J. Margueron, and S. Reddy, Phys. Rev. C **98**, 045804 (2018).
[25] M. W. Coughlin *et al.*, Mon. Not. R. Astron. Soc. **480**, 3871 (2018).
[26] M. W. Coughlin, T. Dietrich, B. Margalit, and B. D. Metzger, Mon. Not. R. Astron. Soc. **489**, L91 (2019).
[27] C. D. Capano, I. Tews, S. M. Brown, B. Margalit, S. De, S. Kumar, D. A. Brown, B. Krishnan, and S. Reddy, Nat. Astron. **4**, 625 (2020).
[28] T. Dietrich, M. W. Coughlin, P. T. H. Pang, M. Bulla, J. Heinzel, L. Issa, I. Tews, and S. Antier, Science **370**, 1450 (2020).
[29] V. Nedora, D. Radice, S. Bernuzzi, A. Perego, B. Daszuta, A. Endrizzi, A. Prakash, and F. Schianchi, Mon. Not. R. Astron. Soc. **506**, 5908 (2021).
[30] S. Huth *et al.*, Nature (London) **606**, 276 (2022).
[31] H. Koehn, T. Wouters, H. Rose, P. T. H. Pang, R. Somasundaram, I. Tews, and T. Dietrich, Phys. Rev. D **110**, 103015 (2024).
[32] H. Koehn *et al.*, Phys. Rev. X **15**, 021014 (2025).
[33] C. Guidorzi *et al.*, Astrophys. J. Lett. **851**, L36 (2017).
[34] K. Hotokezaka, E. Nakar, O. Gottlieb, S. Nissanke, K. Masuda, G. Hallinan, K. P. Mooley, and A. T. Deller, Nat. Astron. **3**, 940 (2019).
[35] M. W. Coughlin, T. Dietrich, J. Heinzel, N. Khetan, S. Antier, M. Bulla, N. Christensen, D. A. Coulter, and R. J. Foley, Phys. Rev. Res. **2**, 022006 (2020).
[36] M. A. Pérez-García *et al.*, Astron. Astrophys. **666**, A67 (2022).
[37] H. Wang and D. Giannios, Astrophys. J. **908**, 200 (2021).
[38] M. Bulla, M. W. Coughlin, S. Dhawan, and T. Dietrich, Universe **8**, 289 (2022).
[39] J. M. Lattimer and D. N. Schramm, Astrophys. J. **192**, L145 (1974).
[40] S. Rosswog, M. Liebendoerfer, F. Thielemann, M. Davies, W. Benz *et al.*, Astron. Astrophys. **341**, 499 (1999).
[41] S. Rosswog, Astrophys. J. **634**, 1202 (2005).
[42] M. Shibata, K. Taniguchi, and K. Uryu, Phys. Rev. D **68**, 084020 (2003).
[43] M. Shibata, K. Taniguchi, and K. Uryu, Phys. Rev. D **71**, 084021 (2005).
[44] L. Rezzolla, L. Baiotti, B. Giacomazzo, D. Link, and J. A. Font, Classical Quantum Gravity **27**, 114105 (2010).
[45] A. Bauswein, S. Goriely, and H.-T. Janka, Astrophys. J. **773**, 78 (2013).
[46] K. Hotokezaka, K. Kiuchi, K. Kyutoku, T. Muranushi, Y.-i. Sekiguchi, M. Shibata, and K. Taniguchi, Phys. Rev. D **88**, 044026 (2013).
[47] T. Dietrich, S. Bernuzzi, M. Ujevic, and B. Brügmann, Phys. Rev. D **91**, 124041 (2015).
[48] T. Dietrich, N. Moldenhauer, N. K. Johnson-McDaniel, S. Bernuzzi, C. M. Markakis, B. Brügmann, and W. Tichy, Phys. Rev. D **92**, 124007 (2015).
[49] S. Bernuzzi and T. Dietrich, Phys. Rev. D **94**, 064062 (2016).
[50] D. Radice, L. Rezzolla, and F. Galeazzi, Mon. Not. R. Astron. Soc. **437**, L46 (2014).
[51] D. Radice, L. Rezzolla, and F. Galeazzi, Classical Quantum Gravity **31**, 075012 (2014).
[52] D. Radice, Astrophys. J. **838**, L2 (2017).
[53] B. Giacomazzo, J. Zrake, P. Duffell, A. I. MacFadyen, and R. Perna, Astrophys. J. **809**, 39 (2015).
[54] D. M. Siegel and R. Ciolfi, Springer Proc. Phys. **170**, 119 (2016).
[55] K. Kiuchi, P. Cerdá-Durán, K. Kyutoku, Y. Sekiguchi, and M. Shibata, Phys. Rev. D **92**, 124034 (2015).
[56] R. Ciolfi, Gen. Relativ. Gravit. **52**, 59 (2020).
[57] C. Palenzuela, R. Aguilera-Miret, F. Carrasco, R. Ciolfi, J. V. Kalinani, W. Kastaun, B. Miñano, and D. Viganò, Phys. Rev. D **106**, 023013 (2022).
[58] K. Kiuchi, A. Reboul-Salze, M. Shibata, and Y. Sekiguchi, Nat. Astron. **8**, 298 (2024).

[59] A. Neuweiler, T. Dietrich, B. Brügmann, E. Giangrandi, K. Kiuchi, F. Schianchi, P. Mösta, S. Shankar, B. Giacomazzo, and M. Shibata, Phys. Rev. D **110**, 084046 (2024).
[60] M. H. Ruffert, H. T. Janka, and G. Schäfer, Astron. Astrophys. **311**, 532 (1996).
[61] S. Rosswog and M. Liebendoerfer, Mon. Not. R. Astron. Soc. **342**, 673 (2003).
[62] Y. Sekiguchi, Classical Quantum Gravity **27**, 114107 (2010).
[63] M. Shibata, K. Kiuchi, Y.-i. Sekiguchi, and Y. Suwa, Prog. Theor. Phys. **125**, 1255 (2011).
[64] F. Foucart, R. Haas, M. D. Duez, E. O'Connor, C. D. Ott, L. Roberts, L. E. Kidder, J. Lippuner, H. P. Pfeiffer, and M. A. Scheel, Phys. Rev. D **93**, 044019 (2016).
[65] L. Lehner, S. L. Liebling, C. Palenzuela, O. L. Caballero, E. O'Connor, M. Anderson, and D. Neilsen, Classical Quantum Gravity **33**, 184002 (2016).
[66] L. Bovard, D. Martin, F. Guercilena, A. Arcones, L. Rezzolla, and O. Korobkin, Phys. Rev. D **96**, 124005 (2017).
[67] F. Foucart, E. O'Connor, L. Roberts, M. D. Duez, R. Haas, L. E. Kidder, C. D. Ott, H. P. Pfeiffer, M. A. Scheel, and B. Szilagyi, Phys. Rev. D **91**, 124021 (2015).
[68] F. Foucart, E. O'Connor, L. Roberts, L. E. Kidder, H. P. Pfeiffer, and M. A. Scheel, Phys. Rev. D **94**, 123016 (2016).
[69] D. Radice, F. Galeazzi, J. Lippuner, L. F. Roberts, C. D. Ott, and L. Rezzolla, Mon. Not. R. Astron. Soc. **460**, 3255 (2016).
[70] D. Radice, A. Perego, K. Hotokezaka, S. A. Fromm, S. Bernuzzi, and L. F. Roberts, Astrophys. J. **869**, 130 (2018).
[71] D. Radice, S. Bernuzzi, A. Perego, and R. Haas, Mon. Not. R. Astron. Soc. **512**, 1499 (2022).
[72] F. Schianchi, H. Gieg, V. Nedora, A. Neuweiler, M. Ujevic, M. Bulla, and T. Dietrich, Phys. Rev. D **109**, 044012 (2024).
[73] D. Radice and S. Bernuzzi, Astrophys. J. **959**, 46 (2023).
[74] R. Bollig, H. T. Janka, A. Lohs, G. Martinez-Pinedo, C. J. Horowitz, and T. Melson, Phys. Rev. Lett. **119**, 242702 (2017).
[75] G. Guo, G. Martínez-Pinedo, A. Lohs, and T. Fischer, Phys. Rev. D **102**, 023037 (2020).
[76] T. Fischer, G. Guo, G. Martínez-Pinedo, M. Liebendörfer, and A. Mezzacappa, Phys. Rev. D **102**, 123001 (2020).
[77] S. L. Shapiro and S. A. Teukolsky, *Black Holes, White Dwarfs, and Neutron Stars: The Physics of Compact Objects* (Wiley, New York, USA, 1983).
[78] N. K. Glendenning, *Compact Stars: Nuclear Physics, Particle Physics, and General Relativity* (Springer, New York, 1997).
[79] P. Haensel, K. Levenfish, and D. Yakovlev, Astron. Astrophys. **357**, 1157 (2000).
[80] P. Haensel, K. P. Levenfish, and D. G. Yakovlev, Astron. Astrophys. **372**, 130 (2001).
[81] M. G. Alford and G. Good, Phys. Rev. C **82**, 055805 (2010).
[82] M. Alford, A. Harutyunyan, and A. Sedrakian, Phys. Rev. D **104**, 103027 (2021).
[83] S. P. Harris, B. Fore, and S. Reddy, Phys. Rev. C **111**, 015802 (2025).
[84] J. M. Lattimer, C. J. Pethick, M. Prakash, and P. Haensel, Phys. Rev. Lett. **66**, 2701 (1991).
[85] E. Loffredo, A. Perego, D. Logoteta, and M. Branchesi, Astron. Astrophys. **672**, A124 (2023).
[86] M. A. Pajkos and E. R. Most, Phys. Rev. D **111**, 043013 (2025).
[87] B. Bruegmann, J. A. Gonzalez, M. Hannam, S. Husa, U. Sperhake, and W. Tichy, Phys. Rev. D **77**, 024027 (2008).
[88] M. Thierfelder, S. Bernuzzi, and B. Brügmann, Phys. Rev. D **84**, 044012 (2011).
[89] H. Gieg, F. Schianchi, T. Dietrich, and M. Ujevic, Universe **8**, 370 (2022).
[90] S. A. Bludman and K. A. van Riper, Astrophys. J. **212**, 859 (1977).
[91] F. X. Timmes and D. Arnett, Astrophys. J. Suppl. Ser. **125**, 277 (1999).
[92] J. M. Aparicio, Astrophys. J. Suppl. Ser. **117**, 627 (1998).
[93] A. Perego, S. Bernuzzi, and D. Radice, Eur. Phys. J. A **55**, 124 (2019).
[94] A. W. Steiner, M. Hempel, and T. Fischer, Astrophys. J. **774**, 17 (2013).
[95] J. A. Font, Living Rev. Relativity **11**, 7 (2008).
[96] F. Galeazzi, W. Kastaun, L. Rezzolla, and J. A. Font, Phys. Rev. D **88**, 064009 (2013).
[97] E. O'Connor and C. D. Ott, Classical Quantum Gravity **27**, 114103 (2010).
[98] E. O'Connor, Astrophys. J. Suppl. Ser. **219**, 24 (2015).
[99] M. B. Deaton, M. D. Duez, F. Foucart, E. O'Connor, C. D. Ott, L. E. Kidder, C. D. Muhlberger, M. A. Scheel, and B. Szilagyi, Astrophys. J. **776**, 47 (2013).
[100] F. Foucart, M. B. Deaton, M. D. Duez, E. O'Connor, C. D. Ott, R. Haas, L. E. Kidder, H. P. Pfeiffer, M. A. Scheel, and B. Szilagyi, Phys. Rev. D **90**, 024026 (2014).
[101] A. Perego, E. Gafton, R. Cabezón, S. Rosswog, and M. Liebendörfer, Astron. Astrophys. **568**, A11 (2014).
[102] A. Perego, R. Cabezon, and R. Kaeppeli, Astrophys. J. Suppl. Ser. **223**, 22 (2016).
[103] C. Palenzuela, S. L. Liebling, D. Neilsen, L. Lehner, O. L. Caballero, E. O'Connor, and M. Anderson, Phys. Rev. D **92**, 044045 (2015).
[104] D. M. Siegel and B. D. Metzger, Astrophys. J. **858**, 52 (2018).
[105] R. Ardevol-Pulpillo, H. T. Janka, O. Just, and A. Bauswein, Mon. Not. R. Astron. Soc. **485**, 4754 (2019).
[106] A. Murguia-Berthier *et al.*, Astrophys. J. **919**, 95 (2021).
[107] P. Anninos and P. C. Fragile, Astrophys. J. **900**, 71 (2020).
[108] M. R. Izquierdo, L. Pareschi, B. Miñano, J. Massó, and C. Palenzuela, Classical Quantum Gravity **40**, 145014 (2023).
[109] F. Foucart, M. D. Duez, F. Hebert, L. E. Kidder, P. Kovarik, H. P. Pfeiffer, and M. A. Scheel, Astrophys. J. **920**, 82 (2021).
[110] K. Kawaguchi, S. Fujibayashi, and M. Shibata, Phys. Rev. D **107**, 023026 (2023).
[111] F. Foucart, M. D. Duez, R. Haas, L. E. Kidder, H. P. Pfeiffer, M. A. Scheel, and E. Spira-Savett, Phys. Rev. D **107**, 103055 (2023).
[112] L. R. Weih, A. Gabbana, D. Simeoni, L. Rezzolla, S. Succi, and R. Tripiccione, Mon. Not. R. Astron. Soc. **498**, 3374 (2020).

[113] M. Cusinato, F. M. Guercilena, A. Perego, D. Logoteta, D. Radice, S. Bernuzzi, and S. Ansoldi, Eur. Phys. J. A **58**, 99 (2022).
[114] D. Neilsen, S. L. Liebling, M. Anderson, L. Lehner, E. O'Connor, and C. Palenzuela, Phys. Rev. D **89**, 104029 (2014).
[115] C. Palenzuela, S. Liebling, and B. Miñano, Phys. Rev. D **105**, 103020 (2022).
[116] M. Rampp and H. T. Janka, Astron. Astrophys. **396**, 361 (2002).
[117] A. Burrows, S. Reddy, and T. A. Thompson, Nucl. Phys. **A777**, 356 (2006).
[118] H. H.-Y. Ng, P. C.-K. Cheong, A. T.-L. Lam, and T. G. F. Li, Astrophys. J. Suppl. Ser. **272**, 9 (2024).
[119] S. W. Bruenn, Astrophys. J. Suppl. Ser. **58**, 771 (1985).
[120] M. Tanabashi *et al.* (Particle Data Group), Phys. Rev. D **98**, 030001 (2018).
[121] G. Martinez-Pinedo, T. Fischer, A. Lohs, and L. Huther, Phys. Rev. Lett. **109**, 251104 (2012).
[122] T. Kuroda, T. Takiwaki, and K. Kotake, Astrophys. J. Suppl. Ser. **222**, 20 (2016).
[123] K. Takahashi, M. F. El Eid, and W. Hillebrandt, Astron. Astrophys. **67**, 185 (1978).
[124] H. Takahasi and M. Mori, Publ. RIMS **9**, 721 (1974).
[125] N. Mohankumar, T. Kannan, and S. Kanmani, Comput. Phys. Commun. **168**, 71 (2005).
[126] W. H. Press, S. A. Teukolsky, W. T. Vetterling, and B. P. Flannery, *Numerical Recipes 3rd Edition: The Art of Scientific Computing*, 3rd ed. (Cambridge University Press, USA, 2007).
[127] L. F. Roberts and S. Reddy, Phys. Rev. C **95**, 045807 (2017).
[128] M. Oertel, A. Pascal, M. Mancini, and J. Novak, Phys. Rev. C **102**, 035802 (2020).
[129] T. Fischer, G. Guo, A. A. Dzhioev, G. Martínez-Pinedo, M.-R. Wu, A. Lohs, and Y.-Z. Qian, Phys. Rev. C **101**, 025804 (2020).
[130] A. Endrizzi, A. Perego, F. M. Fabbri, L. Branca, D. Radice, S. Bernuzzi, B. Giacomazzo, F. Pederiva, and A. Lovato, Eur. Phys. J. A **56**, 15 (2020).
[131] C. Sullivan, E. O'Connor, R. G. T. Zegers, T. Grubb, and S. M. Austin, Astrophys. J. **816**, 44 (2016).
[132] T. Suzuki, H. Toki, and K. Nomoto, J. Phys. Soc. Jpn. Conf. Proc. **14**, 020402 (2017).
[133] T. Oda, M. Hino, K. Muto, M. Takahara, and K. Sato, Atom. Data Nucl. Data Tables **56**, 231 (1994).
[134] K. Langanke, G. Martinez-Pinedo, J. M. Sampaio, D. J. Dean, W. R. Hix, O. E. B. Messer, A. Mezzacappa, M. Liebendoerfer, H. T. Janka, and M. Rampp, Phys. Rev. Lett. **90**, 241102 (2003).
[135] K. Langanke and G. Martinez-Pinedo, Nucl. Phys. **A673**, 481 (2000).
[136] F. Zappa, S. Bernuzzi, D. Radice, and A. Perego, Mon. Not. R. Astron. Soc. **520**, 1481 (2023).
[137] C. Horowitz, Phys. Rev. D **65**, 043001 (2002).
[138] W. Tichy, Classical Quantum Gravity **26**, 175018 (2009).
[139] W. Tichy, Phys. Rev. D **86**, 064024 (2012).
[140] W. Tichy, A. Rashti, T. Dietrich, R. Dudi, and B. Brügmann, Phys. Rev. D **100**, 124046 (2019).
[141] M. G. Alford, L. Brodie, A. Haber, and I. Tews, Phys. Rev. C **106**, 055804 (2022).
[142] M. J. Berger and J. Oliger, J. Comput. Phys. **53**, 484 (1984).
[143] S. Bernuzzi and D. Hilditch, Phys. Rev. D **81**, 084003 (2010).
[144] D. Hilditch, S. Bernuzzi, M. Thierfelder, Z. Cao, W. Tichy, and B. Brügmann, Phys. Rev. D **88**, 084057 (2013).
[145] M. Campanelli, C. O. Lousto, P. Marronetti, and Y. Zlochower, Phys. Rev. Lett. **96**, 111101 (2006).
[146] C. Bona, J. Masso, E. Seidel, and J. Stela, Phys. Rev. Lett. **75**, 600 (1995).
[147] M. Alcubierre, B. Brügmann, P. Diener, M. Koppitz, D. Pollney, E. Seidel, and R. Takahashi, Phys. Rev. D **67**, 084023 (2003).
[148] R. Borges, M. Carmona, B. Costa, and W. S. Don, J. Comput. Phys. **227**, 3191 (2008).
[149] A. Harten, P. D. Lax, and B. v. Leer, SIAM Rev. **25**, 35 (1983).
[150] E. F. Toro, *Riemann Solvers and Numerical Methods for Fluid Dynamics* (Springer-Verlag, Berlin, 1999).
[151] S. Bernuzzi, A. Nagar, M. Thierfelder, and B. Brügmann, Phys. Rev. D **86**, 044030 (2012).
[152] T. A. Thompson, A. Burrows, and J. E. Horvath, Phys. Rev. C **62**, 035802 (2000).
[153] K. Hotokezaka, K. Kiuchi, K. Kyutoku, H. Okawa, Y. Sekiguchi, M. Shibata, and K. Taniguchi, Phys. Rev. D **87.2**, 024001 (2013).
[154] B. Fore and S. Reddy, Phys. Rev. C **101**, 035809 (2020).
[155] V. Vijayan, N. Rahman, A. Bauswein, G. Martínez-Pinedo, and I. L. Arbina, Phys. Rev. D **108**, 023020 (2023).